CONTENTS

	Page
SUMMARY	1
INTRODUCTION	1
SYMBOLS	2
STATEMENT OF THE PROBLEM	7
DEFINITION OF KEY PARAMETERS	9
Image Resolution	9
Effect of Astigmatism on Image Distance	10
Binocular Considerations	12
RESULTS AND DISCUSSION	13
Dot Ray Tracing	13
Astigmatism	14
Image Distance	14
Binocular Disparity	14
Magnification Differences	15
Results of Design Study	15
Summary of Results	16
CONCLUDING REMARKS	16
APPENDIX A - DEVELOPMENT OF AN ACHROMATIC DESIGN	18
Geometrical Ray Tracing	19
Details of Design Procedure	21
APPENDIX B - RELATIONSHIP OF ABERRATION CURVES TO IMAGE DISTANCE	25
REFERENCES	30
TABLES	31
FIGURES	35

NAS 1.60: 1066

DEC 1 1977

NASA Technical Paper 1066

COMPLETED
ORIGINAL

Analysis and Design of a Refractive Virtual Image System

William M. Kahlbaum, Jr.

NOVEMBER 1977

NASA

77

NAS 1.60:1066

NASA Technical Paper 1066

Analysis and Design of a Refractive Virtual Image System

William M. Kahlbaum, Jr.
Langley Research Center
Hampton, Virginia

NASA
National Aeronautics
and Space Administration

Scientific and Technical Information Office

1977

SUMMARY

This paper describes the development of analytical tools for evaluating the optical performance of a virtual image display system. Observation of a two-element (unachromatized doublet) refractive system led to the conclusion that the major source of image degradation was lateral chromatic aberration. This conclusion was verified by computer analysis of the system. The lateral chromatic aberration is given in terms of the resolution of the phosphor dots on a standard shadow mask color cathode ray tube (CRT). Single wavelength considerations include: astigmatism, apparent image distance from the observer, binocular disparities and differences of angular magnification of the images presented to each of the observer's eyes. Where practical, these results are related to the performance of the human eye. All these techniques are applied to the previously mentioned doublet and a triplet (three-element) refractive system. The triplet (a result of the design procedure described in an appendix) provides a 50-percent reduction in lateral chromatic aberration which was the design goal. Distortion was also reduced to a minimum over the field of view.

The methods used in the design of the triplet are presented along with a method of relating classical aberration curves to image distance and binocular disparity. The triplet system has been fabricated and is currently being used to provide a simulated "out the window" display for aeronautical researchers at Langley Research Center.

INTRODUCTION

Virtual image viewing systems have been used to provide realistic visual cues in flight simulators for a number of years. Basically, such a system consists of a series of lenses and/or mirrors located between the observer and an image source which is normally a closed circuit television monitor. This system magnifies the image and makes it appear to be at a large distance, preferably at infinity, but normally greater than 5 m. The magnification provides more eye relief between the observer and the first optical element than would exist between the observer and a directly viewed television monitor for the same visual field angle. Projecting the image to a large distance (collimation) provides less eye strain and a more relaxed state of accommodation and convergence of the observer's eyes.

One of the simplest and the most economical type of system consists of several large diameter plastic lenses placed between the observer and the television monitor, the monitor being located at or inside the focal point of the lens combination. This location provides the observer with a virtual image which appears to be at (or close to) infinity. A very common form of this type of system, which provides satisfactory results, consists of two plano-convex lenses arranged with the two convex surfaces facing each other. This system is referred to hereafter as the doublet. This arrangement allows lower f-numbers

to be achieved than in the case of a single lens and also reduces some of the monochromatic aberrations of the system.

Such a system has been in use at the Langley Research Center for several years. In the interest of providing improved image quality, a study was undertaken to evaluate current system performance and investigate possible improvements. The analytical evaluation phase of the study was accomplished by using a modified version of the POLYPAGOS (ref. 1) ray tracing computer program to trace bundles of rays from the cathode ray tube (CRT) faceplate through the system to the eye point of the observer. Differences of ray inclination angles with respect to the optic axis, as the rays pass through the center and edge of the eye pupil, were determined. These angular differences vary as a function of field angle and head position in the system exit pupil and can be related to astigmatism and apparent image distance for a one-eyed observer and binocular disparity and magnification differences for the two-eyed observer. In the course of these studies, it was found that the primary cause of image degradation in the doublet occurred at larger field angles and was primarily a problem of lateral chromatic aberration. A modification of the analysis was used to evaluate the chromatic aberration, and an effort was undertaken to design a triplet lens which would reduce the chromatic aberrations. Classical design techniques were used although some modifications were necessary to fit the nature of the problem. These methods and modifications are described in more detail.

This report deals primarily with the ray trace analyses of both the doublet and triplet systems. These analyses include the development of methods and presentation of results concerning image resolution, image distance, binocular disparities, and magnification differences. Appendices A and B deal with the methods used in the triplet design and the relationship between the classical aberration curves and collimation of the visual field.

A prototype of the achromatic system was built and used to verify the analytical data. An operational version of the achromat has been assembled and used in a visual landing simulator at Langley Research Center since July 1976.

SYMBOLS

a	a distance equal to one-half of interocular distance, cm
B_1^*, B_2^*, B_3^*	third-order thin-lens approximation of spherical aberration of first, second, and third lenses, respectively, cm
C	position of CRT at axial focal point of lens, cm
C'	position of CRT when displaced inside axial focal point of lens, cm
C_2, C_4, C_6	first surface curvature of first, second, and third lenses, respectively

C_1^*, C_2^*, C_3^*	third-order thin-lens approximation of astigmatism of first, second, and third lenses, respectively, cm
D	abbreviation for diopter which is unit of refractive power of a lens, m^{-1}
D_m	percentage difference of angular magnification between two eyes, dimensionless
D_o	diameter of individual wavelength dot image, cm
D_1	length of chromatically aberrated dot image, cm
E	elongation of dot image, dimensionless
E_1^*, E_2^*, E_3^*	third-order thin-lens approximation of distortion of first, second, and third lenses, respectively, cm
F_1^*, F_2^*, F_3^*	third-order thin-lens approximation of coma of first, second, and third lenses, respectively, cm
f_B	back focal length of lens, cm
f_L	focal length of lens, cm
f_m	focal length of mirror, cm
ID_{av}	average image distance, m
ID_o	axial average image distance, m
ID_{SA}	estimated sagittal image distance for case A based on slope of aberration curve of Y_s against X_E, m
ID_{TA}	estimated tangential plane image distance for case A based on slope of aberration curve of Y_T against Y_E, m
M	average focal surface, cm
M_A	angular magnification, dimensionless
M_{AL}	angular magnification in left eye, dimensionless
M_{AR}	angular magnification in right eye, dimensionless
P	Petzval surface, cm
P_C	Petzval sum aberration coefficient, cm
R	parameter proportional to ratio of spacing between lenses 1 and 2 and 2 and 3

r	coordinate position in the entrance pupil, cm
S	sagittal focal surface, cm
S_I	sagittal image distance, m
S_1, S_2	designates two rays in sagittal fan, dimensionless
s, s'	denotes paraxial object and image distances, cm
T	tangential focal surface, cm
T_I	tangential image distance, m
T_1, T_2	designates two rays in tangential fan, cm
t_i	separation between ith and (i + 1)th thin lens, cm
t_{K1}	distance from paraxial focal point of lens to object when object is located outside of focal point, cm
t_{K2}	distance from paraxial focal point of lens to object when object is located inside of focal point, cm
X_E, Y_E	coordinates of any ray as it intersects entrance pupil, cm
X_{en}, Y_{en}, Z	an axis system centered in entrance pupil of system, dimensionless
X_{ex}, Y_{ex}, Z	an axis system centered in exit pupil of system, dimensionless
X_I, Y_I, Z	an axis system centered in image plane of perfect surface, dimensionless
X_L, Y_L, Z	an axis system located at center of a thin lens with a focal length equal to that of lens being studied, dimensionless
X_o, Y_o, Z	an axis system centered on CRT, dimensionless
X_{ps}, Y_{ps}, Z	an axis system centered in perfect surface, dimensionless
X_s, Y_s	vertical and horizontal displacement of a ray in sagittal fan measured relative to chief ray on surface of CRT, cm
X_T, Y_T	vertical and horizontal displacement of a ray in tangential fan measured relative to chief ray on surface of CRT, cm
X_v, Y_v, Z	an axis system in plane containing best focus point of virtual image, dimensionless
Z	defines optical axis of system, dimensionless

Z_o distance from primary principal plane of lens system to observer, cm

dY_T/dY_E slope of aberration curve of Y_T against Y_E, dimensionless

dX_S/dX_E slope of aberration curve of X_S against X_E, dimensionless

α_L, α_R azimuth angles of chief rays passing through left and right eye pupils, respectively, measured relative to X_{ex}, Y_{ex}, Z axis system, radians

$\alpha_{11}^*, \alpha_{12}^*, \alpha_{13}^*$ first spherical aberration coefficient for lenses 1, 2, and 3, respectively, cm

$\alpha_{21}^*, \alpha_{22}^*, \alpha_{23}^*$ second spherical aberration coefficient for lenses 1, 2, and 3, respectively, cm^2

$\alpha_{31}^*, \alpha_{32}^*, \alpha_{33}^*$ third spherical aberration coefficient for lenses 1, 2, and 3, respectively, cm^3

β_L, β_R elevation angles of chief rays passing through left and right eye pupils, respectively, measured relative to X_{ex}, Y_{ex}, Z axis system, radians

$\beta_{11}^*, \beta_{12}^*, \beta_{13}^*$ first coma coefficient for lenses 1, 2, and 3, respectively, cm

$\beta_{21}^*, \beta_{22}^*, \beta_{23}^*$ second coma coefficient for lenses 1, 2, and 3, respectively, cm^2

$\beta_{31}^*, \beta_{32}^*, \beta_{33}^*$ third coma coefficient for lenses 1, 2, and 3, respectively, cm^3

$\gamma_{11}^*, \gamma_{12}^*, \gamma_{13}^*$ first astigmatism coefficient for lenses 1, 2, and 3, respectively, cm

$\gamma_{21}^*, \gamma_{22}^*, \gamma_{23}^*$ second astigmatism coefficient for lenses 1, 2, and 3, respectively, cm^2

$\gamma_{31}^*, \gamma_{32}^*, \gamma_{33}^*$ third astigmatism coefficient for lenses 1, 2, and 3, respectively, cm^3

Δa measure of aberration in any direction in plane of CRT used in derivation of relationship between aberration amplitude and either image distance or binocular disparity, cm

ΔP average value of ΔS and ΔT, diopters (m^{-1})

Δr displacement in entrance pupil, cm

ΔS sagittal equivalent refractive power, diopters (m^{-1})

ΔT tangential equivalent refractive power, diopters (m^{-1})

ΔU_{SB}	horizontal binocular disparity for case B, radians
ΔU_{TA}	horizontal binocular disparity for case A, radians
ΔU_{TB}	vertical binocular disparity for case B, radians
$\Delta X_1, \Delta X_2$	sagittal components of CRT plane intercepts of rays in tangential fan, cm
$\delta_{11}^*, \delta_{12}^*, \delta_{13}^*$	first distortion coefficient for lenses 1, 2, and 3, respectively, cm
$\delta_{21}^*, \delta_{22}^*, \delta_{23}^*$	second distortion coefficient for lenses 1, 2, and 3, respectively, cm^2
$\delta_{31}^*, \delta_{32}^*, \delta_{33}^*$	third distortion coefficient for lenses 1, 2, and 3, respectively, cm^3
θ_F	half field angle, radians or degrees
θ_I	angle subtended by image points in definition of angular magnification, radians
θ_o	angle subtended by object points in definition of angular magnification, radians
λ_1	peak wavelength of CRT phosphor spectral intensity curve, Å
λ_2, λ_3	half intensity wavelength of CRT phosphor spectral intensity curve, Å
ρ_i	curvature of ith surface, 1/cm
ΣB	sum of third-order thin-lens contributions of spherical aberration for all three lenses, cm
ΣC	sum of third-order thin-lens contributions of astigmatism for all three lenses, cm
ΣE	sum of third-order thin-lens contributions of distortion for all three lenses, cm
ΣF	sum of third-order thin-lens contributions of coma for all three lenses, cm
Φ	optical invariant, cm

Subscripts:

max	maximum value
1,2,. . .	specific values of parameters

Definition of Terms

convergence — the binocular condition of the observer's eyes in the horizontal plane where the eyes are pointing toward each other

dipvergence — a vertical difference in the pointing direction of the observer's two eyes

divergence — the binocular condition of the observer's eyes in the horizontal direction where the eyes are pointing away from each other

V number — a number proportional to the reciprocal of the chromatic dispersion of an optical material

STATEMENT OF THE PROBLEM

The refractive doublet and the reflective types of virtual image systems are shown schematically in figure 1. The refractive type of system has the advantages of generally being smaller, lighter in weight, and having a higher light transmission characteristic. Also wide horizontal fields of view can be achieved by abutting several systems together. The primary disadvantage of the refractive system is its optical performance especially in the area of chromatic aberrations. Most refractive systems are made of plastic rather than of glass because of lower cost and weight. Consideration of weight is especially important if the system is to be used on a moving-base flight simulator. The use of plastic in an achromatic refractive system has one distinct design disadvantage in that only two types of material are readily available. Acrylic has a high V number whereas polystyrene has a low V number. Thus, achromatization is possible but a wide choice of different indices (and hence dispersions) is not available as a degree of freedom in the design. Another minor disadvantage of plastic is that it is much more susceptible to surface scratches.

The ideal virtual image system is perfectly collimated to infinity so that any light ray from any object point on the CRT will emerge from the system parallel to all other rays which originate at that same point. If this situation exists, then the observer's eyes are accommodated and converged to infinity which is the most relaxed condition. This situation would exist for any lateral displacement of the two eye pupils of an observer anywhere within a prescribed system exit pupil. (See fig. 2.) For any lens system there are positions of the CRT which at least partially meet this ideal situation. If the axial point of the CRT is positioned at the focal point as was shown in figure 1 and position C of figure 2, then only the axial point is collimated to infinity. As off-axis points of the lens are considered, several focal surfaces are generated and partial collimation occurs only for points on these surfaces when all other aberrations are ignored. The effects of these other aberrations are considered later. Two of these focal surfaces: the tangential (T) and the sagittal (S) are characteristic of astigmatism. (See fig. 2.) For a cone-shaped bundle of rays originating on the T surface, only those rays in the tangential plane are collimated whereas for the S surface only those rays in the sagittal plane are collimated. Those rays originating from T and S that are not collimated will either diverge from a virtual image or converge to

a real image. A bundle of rays originating from M, which is halfway between the T and S surfaces and corresponds to the best focal surface, will either diverge or converge uniformly from or to some point other than infinity. If astigmatism were reduced to zero, then all three surfaces T, S, and M would coincide at the Petzval surface (P). For this condition all rays starting from the P surface would be uniformly collimated at infinity. In all the cases considered, the effect of other aberrations (spherical and coma) would be to vary the degree of collimation over the system exit pupil.

An axial position of the CRT between any of the surfaces described and the lens will provide bundles of light rays diverging from a virtual image in front of the observer, whereas positions outside of these surfaces will provide bundles converging to a real image behind the observer. Since the surfaces and the CRT curve in opposite directions, it is necessary to displace the axial point of the CRT inside the paraxial focus to location C' in figure 2 in order to provide a virtual image over most of the field of view. Placing the CRT about 7.5 cm inside the axial focal point gives an axial image distance of 5 m and an infinite image distance at a half field angle of $\theta_F = 15^\circ$. This position of the CRT relative to the focal point was used in the analysis of both the doublet and triplet system.

Close observation of the CRT image through the doublet refractive system revealed the most obvious flaw in the performance to be a gradual blurring of the image with increasing half field angle θ_F. Ganzler refers to this problem qualitatively. (See ref. 2.) When using a conventional shadow mask color CRT with the doublet lens, this blurring shows up as a gradual lengthening of the phosphor dots in the radial direction until for θ_F of approximately 7°, adjacent like-color dots completely overlap each other to form radial lines. This condition is especially evident when a blank raster is viewed through a telescope with only the green phosphor energized. This condition results from a relative displacement of the images of the dots at different wavelengths in the spectrum of the phosphor, and the displacement is caused by the lateral chromatic aberration of the system.

The assessment of image distance and binocular disparity becomes meaningless when the image is badly blurred. Thus, the main thrust of the design effort has been to improve image resolution by reducing chromatic aberrations, and at the same time attempt to insure that image distance and binocular disparity do not exceed the limits of comfortable viewing. A triplet design was chosen because of its capability to reduce chromatic aberrations. Also the triplet is a simple design and many of the classical design techniques for this type of lens can be used. A few modifications of the classical techniques were necessary to fit the present situation and these are discussed later. Finally, the triplet can be thought of as the doublet system with an additional color-correcting element inserted between the two elements.

An achromatic doublet (this is different from the previously mentioned doublet) could not be used to provide the desired achromatization because for the combination of power and lens diameter required, the center thickness would be prohibitive.

DEFINITION OF KEY PARAMETERS

Image Resolution

The observed loss of image resolution was analyzed by a brute-force ray tracing method. The phosphor dots on the color CRT provided a convenient resolution target for both observation and analysis. Also the phosphor dots contain the spectral content necessary to demonstrate the chromatic aberrations of the system. The theoretical analysis consisted of tracing bundles of rays from points on the phosphor dots (on the inner surface of the CRT) through the optical system and finally through an aberration-free "perfect" surface located in the system exit pupil. The perfect surface was an aberration-free optical surface which converged the rays to form a real image of the dot. Figure 3 illustrates the orientation of individual rays in the bundle of rays originating from a single point on one phosphor dot as they traverse the system to the final image. The rays entering the system entrance pupil at points A, B, C, D and P pass through the system exit pupil and enter the perfect surface at points A', B', C', D', and P', respectively. Figure 4 defines the points of origin of each of the ray bundles which make up the images of two adjacent like-color phosphor dots.

The shape of the dot image at a single wavelength is an indication of the monochromatic aberrations, whereas the relative displacements of the dot images at several wavelengths indicate the chromatic aberrations. A telescope was used to observe the dots through the system because the angle subtended by individual dots is very close to the limiting resolution of the eye. The objective lens of the telescope was masked down to a diameter of 0.5 cm to reduce the effects of its aberrations and, as a result, more closely approximate the perfect surface used in the theoretical studies. This same size aperture was used in the theoretical studies to allow a correlation between the theoretical and experimental results.

Ray tracing from all points on a single dot was repeated at three wavelengths for blue and green only: one at the peak wavelength of the phosphor spectral output curve λ_1 and one at each of the two half intensity points λ_2 and λ_3. (See fig. 5.) Ray tracing at only one wavelength in red was sufficient since the red phosphor is essentially monochromatic. (See fig. 6.) The relative positions of the images of like-color dots were plotted as shown in figure 7. The position of the image at the peak wavelength λ_1 was used as the reference point. The elongation of any dot image may be expressed as

$$E = \frac{D_1}{D_o} \tag{1}$$

where

D_1 length of chromatically aberrated dot image

D_o diameter of individual wavelength dot image

This chromatically induced elongation of the dot image increases as a function of field angle, and adjacent like-color dot images are no longer resolvable after they touch.

To determine the value of E at which resolution is lost, consider the standard pattern of phosphor dots illustrated in figure 8(a). The chromatically elongated images of two adjacent green dots G-1 and G-2 are shown in figure 8(b). It can be seen in this figure that resolution will be lost in the horizontal direction when $E = 3$ and the images touch. A similar figure could be drawn for the vertical direction where resolution is lost when $E = 1.732$. Because of the monochromatic nature of the red phosphor, there is no elongation of the red dots and they are distinguishable over the whole field of view.

Effect of Astigmatism on Image Distance

The determination of apparent image distance over the field of view is a major concern in the analysis of these systems. The method used consists of tracing bundles of rays from a point on the CRT through the system and then to the observer's eye pupil. Figure 9 illustrates the geometry involved. The slopes of the incident rays from O through points A, B, C, and D are adjusted so that the emerging rays pass through the edges of the eye pupil at points A', B', C', and D', respectively. In the absence of astigmatism all emerging rays will diverge from or converge to a single minimum best focus point. This point is determined in the computations by longitudinally translating the image plane containing this best focus point until the area of intersection of the bundle with that plane is a minimum. Variations of field angle are accomplished by changing the height of the object point, whereas variations of head position are accomplished by moving the eye pupil horizontally or vertically over the area defined by the system exit pupil.

The complete absence of astigmatism is satisfied only for the case of zero field angle and zero eye displacement. Astigmatism is introduced in the emerging bundle of rays whenever the eye pupil moves off axes. As a result of this, the rays in the tangential fan diverge from or converge to a different point than those in the sagittal fan. The image distance for each fan of rays as a function of eye position at each field angle was determined separately by using the techniques described. Plots were made of the equivalent refractive power of the lens in the tangential ΔT and sagittal ΔS planes. This equivalent power is related to image distances as follows:

$$\Delta T = \frac{1}{ID_O} - \frac{1}{T_I} \tag{2}$$

$$\Delta S = \frac{1}{ID_O} - \frac{1}{S_I} \tag{3}$$

where

T_I tangential image distance from observer to best focus point

S_I sagittal image distance from observer to best focus point

ID_o image distance from observer to best focus point for zero field angle and eye displacement

Typical plots of ΔT and ΔS are shown in figure 10 which treats the case of zero field angle. The technique of analyzing astigmatism used here is similar to that used in the design of spectacle lenses where $\Delta T - \Delta S$ is the measure of astigmatism. (See ref. 3.) The advantage of using reciprocals in this analysis is that the scales of the plots are more manageable, especially at large image distances. In the design of spectacle lenses, the limit of $\Delta T - \Delta S$ is normally set between 0.1 and 0.2 diopter (D). The limit of 0.2D was adopted here which imposed a limit of ± 6 cm on eye displacement because of the magnitude of $\Delta T - \Delta S$ at larger field angles. (See section "Results and Discussion.") This condition results in a limit of ± 3 cm of head motion when an interocular distance of 6.4 cm is assumed.

Simple astigmatism as treated thus far assumes that rays in the emerging tangential fan have no out-of-plane or sagittal components and that emerging sagittal rays have no tangential components. As long as the eye displacement is in the same plane as the field angle, this restriction is satisfied. This condition is defined as case A. Considering a two-eyed observer and allowing head displacement in the X-direction while still observing a point on the Y-axis (defined as case B) leads to a situation where the emerging tangential rays have a sagittal component and vice versa for the sagittal fan. This twisting of the two fans of rays is illustrated in figure 11 which treats the situation of the tangential fan of rays with ΔX_1, and ΔX_2 representing the sagittal components. The image distance can still be determined by using the techniques outlined but application of the maximum limits becomes uncertain as the out-of-plane component increases. It cannot be readily determined what effects the twisting of the bundle would have on the observer's acuity without becoming deeply involved in human factors aspects. This question has not been approached and for the purposes intended here, only case A will be considered in establishing the level of astigmatism present.

The average image surface which is conjugate to the M surface of figure 2 is located halfway between the tangential and sagittal image surfaces and is defined in figure 10 as

$$\Delta P = \frac{\Delta T + \Delta S}{2} \tag{4}$$

Average image distance is defined as

$$ID_{av} = \frac{T_I + S_I}{2} \tag{5}$$

Writing equation (5) in terms of the reciprocal of average image distance gives

$$\frac{1}{ID_{av}} = \frac{2}{T_I + S_I} \tag{6}$$

Substituting equations (2), (3), and (4) into equation (6) gives

$$\frac{1}{ID_{av}} = \frac{\left(\frac{1}{ID_o} - \Delta T\right)\left(\frac{1}{ID_o} - \Delta S\right)}{\frac{1}{ID_o} - \Delta P} \tag{7}$$

Equation (7) now provides a means of determining average image distance from astigmatism curves such as figure 10. Tabulated values of maximum variations of $1/ID_{av}$ as a function of field angle and eye position were determined and plotted.

Binocular Considerations

In dealing with binocular vision several parameters must be considered. Binocular fusion is lost if there is an excessive angular difference between the directions in which the two eyes are forced to point or there is an excessive difference in the angular magnification of the image presented to each eye.

Figure 12 illustrates the geometry involved in the study of pointing differences between the two eyes. A chief ray is traced from the object point through the system to the center of each eye aperture. The difference in horizontal slopes $\alpha_L - \alpha_R$ is a measure of horizontal disparity and the difference in vertical slopes $\beta_L - \beta_R$ is a measure of vertical disparity. Note here that angles measured upward and to the right are positive. Also divergence is indicated by a positive value of $\alpha_L - \alpha_R$.

Angular magnification for the chief rays traced from each of two closely separated points on the CRT to the center of the eye aperture may be defined in figure 13 as

$$M_A = \frac{\theta_I}{\theta_o} \tag{8}$$

where

θ_o angle subtended by object points

θ_I angle subtended by corresponding image points

The percentage difference in angular magnification is expressed as

$$D_m = 2\,\frac{M_{AR} - M_{AL}}{M_{AR} + M_{AL}} \times 100 \qquad (9)$$

The subscripts R and L refer to the right and left eye, respectively.

The horizontal and vertical disparities and the angular magnification differences were analyzed for two geometrical relationships between the observer's eye pupils and the field angle direction. In case A the field angle is measured in a plane containing the line between the two eyes whereas in case B the field angle is measured in a plane perpendicular to this same line. Rays are traced from an object point on the $+Y_o$ axis and intersect the system exit pupil along both the $\pm X_{ex}$ and the $\pm Y_{ex}$ axes. (See fig. 14.) With the use of this one set of ray trace data, case A is treated by positioning the eye pupils along the $\pm Y_{ex}$ axis and case B by positioning the eye pupils along the $\pm X_{ex}$ axis. Case B is particularly important since it represents the major area of interest in a landing simulator.

RESULTS AND DISCUSSION

The results fall into three main categories: (1) The dot ray tracing which is basically the resolution analysis, (2) the effects of astigmatism, image distance, and binocular analysis, and (3) the results of the design phase. In all three areas a comparison is made between the doublet and triplet systems. The dot ray tracing results show the degree of reduction in lateral chromatic aberration. In the image distance calculations, only case A was studied. Case B was not studied because of the previously described twisting of the ray bundles as they enter the eye pupil. In the binocular studies, both cases A and B were considered because only the chief ray through the center of each eye pupil was considered. The binocular studies include the effects of eye pointing disparities (convergence, divergence, and dipvergence) and the effects of magnification differences between the two eyes. The results of the design phase include data concerning the improvement of lateral chromatic aberration and distortion and curves describing a slight degradation of the monochromatic aberrations over the system entrance pupil which has an effect on collimation.

Dot Ray Tracing

The dot ray tracing was carried out for the two systems. Figure 15 shows a plot of dot elongation E as a function of half field angle for both systems. The achromatized system shows a 50-percent reduction in the value of E at any field angle which was the target value in the design phase. In effect, this means that the field angle at which the loss of resolution of individual dots occurs has been doubled. This result was confirmed by observation.

A disagreement does appear between the analytical and measured value of field angle at which the dots overlap. The analytical results indicate a

larger angle at which overlap occurs. This can only be explained by noting that the analytical results correspond to a smaller spectral width than actually exists, so that overlap contributions due to wavelength components outside of the half intensity points do not show up in the analytical results. This condition results in a smaller apparent overlap at any field angle, but does not affect the comparison between the two systems since this same effect will be present in the analyses of both systems.

Astigmatism

Plots of equivalent refractive power, previously described, were plotted for systems at each field angle as a function of lateral eye position, for case A only. (See figs. 16 and 17.) The field angle varied from 0° to 15° in 5° increments. Use of the 0.2D limit on astigmatism limited the lateral eye displacement to be no greater than ± 6 cm over the whole field of view. Note that the limiting value of 0.2D is approached only at the 10° half field angle for the triplet system. Even though the performance of the triplet system is worse than that of the classical system, it is still within the chosen tolerance. Further, it appears that the limit of 0.2D of astigmatism may be too restrictive in dealing with a biocular system such as this. The reason for the conclusion is that a subjectively satisfactory image is achieved in the prototype system for regions of eye motion where the limit is exceeded.

Image Distance

The average image distance has been previously defined as being halfway between the tangential and sagittal image surfaces. Plots of $1/ID_{av}$ from equation (7) were made for both systems and for case A only. (See figs. 18 and 19.) These curves are for a single eye only. Note that image distance starts at 5 m for zero field angle and eye displacement. For zero eye displacement, it increases toward infinity as the field angle increases. At 10° and 15°, the image distance approaches infinity as the right eye approaches maximum allowable displacement, as indicated by the $1/ID_{av}$ curve approaching zero. An increase of image distance for all field angles could be obtained by moving the CRT closer to the focal point. As a result, all the curves would be forced downward toward an infinite image distance but a larger portion of the higher field angle curves would lie in the region of real image designated by negative values of $1/ID_{av}$. It was the trade-off between maximum image distance at zero field angle and not allowing the image to become real that dictated the final position of the CRT. In the doublet system the CRT could be pushed closer to the focal point since the curves are flatter as shown in figure 19, but it was decided to make the axial image points of both systems equal for purposes of comparison.

Binocular Disparity

The horizontal binocular disparities of the triplet and doublet lenses for cases A and B are compared in figure 20. With the observer's head displaced laterally by ± 3 cm, assuming an interocular distance of 6 cm, one eye was posi-

tioned at the limiting value of ±6 cm which was the limit used in the image distance calculations. For the condition of 0° field angle and zero head displacement, the horizontal disparity in case A for either system is 42 arc minutes. This agrees with the average image distance for either eye as was shown in figure 18 or 19. Therefore, the accommodation and convergence cues are in complete agreement. In case A, as the head displacement and/or field angle change, the horizontal disparity follows the curves in figure 20. For a given head position, each eye will be accommodated at a different distance as illustrated in figure 18 or 19. As a result, it is no longer a simple matter to relate the accommodation and convergence status of the eyes. Studies of the human binocular mechanism (see ref. 4) have shown that there can be a certain amount of disagreement between the two stimuli and still maintain binocular fusion. No analysis has been made to see whether the data described above falls within the acceptable limits referred to in reference 4. The horizontal disparity curves for case B are also shown in figure 20. No comparison can be made between accommodation and convergence because of the lack of reliable image distance information as was previously mentioned.

The case of vertical disparity is somewhat simpler. The normal situation is one of zero disparity and the normally accepted limit is 17 arc minutes. (See ref. 5.) Plots of vertical disparity for cases A and B in both systems are shown in figure 21. The data are plotted as a function of head position and half field angle. At no point does the vertical disparity exceed the 17-arc-minute limit.

All the binocular data show a higher level of disparity for the triplet when compared with the doublet. Even higher values were encountered for larger head displacements than those used in the figures. In spite of this, at no point has a loss of binocular fusion been encountered, even for the larger values of head displacement mentioned.

Magnification Differences

Figure 22 shows a comparison of the percentage difference of the angular magnification presented to each eye for cases A and B and both systems. Reference 5 places a limit of a 2-percent difference in a binocular system. The figure shows a magnification difference as high as 15 percent, but there has been no resulting loss of binocular fusion. No explanation is offered for this difference except to note that in this system both eyes are sharing the same field of view, whereas in a binocular system each eye has a separate field. Also in a binocular the eyes are normally accommodated to infinity, whereas in these systems the accommodation is as shown in figures 18 and 19.

Results of Design Study

The system which resulted from the design study is described in figure 23 and table I. In table I the indices of refraction refer to the material to the right of a particular surface. Three standard optical performance criteria (ref. 5) were used in arriving at this design. They are lateral chromatic aberration (fig. 24), fractional distortion (fig. 25), and the monochromatic

aberration curves (figs. 26 and 27). The same data for the doublet are also presented in these figures as a basis for comparison of the two systems. Appendix A describes the desired shape of the monochromatic aberration curves. Figures 24 and 25 show that the chromatic aberration and distortion of the triplet are less than the doublet. Figures 26 and 27 show an increase in the difference between the tangential and sagittal aberration curves for the triplet. This increase causes a wider fluctuation of horizontal binocular disparities as is described in appendix A and confirmed by figure 20.

Summary of Results

A summary of the results is shown in tables II to V. Table II shows the maximum astigmatism encountered at each field angle. Table III shows the maximum value of horizontal disparity and table IV the maximum value of vertical disparity encountered at each field angle. Table V shows the maximum differences of magnification encountered at each field angle. Tables III to V show data for both cases A and B. The maximum values in these tables are for any point within the allowed limit of eye or head displacement.

CONCLUDING REMARKS

This report has described the development of analytical tools for use in the evaluation of virtual image systems. Two systems have been analyzed by using these techniques. The first was a doublet system and the second was a triplet system, the design of which is described in appendix A. Subjective evaluation of the observed scene reveals a marked improvement of the triplet over the doublet. Specifically, the lateral chromatic aberration has been reduced by one-half which means that a fixed spacing resolution target (the color phosphor dots on the shadow mask color CRT) can be resolved over twice as much of the field of view.

Pincushion distortion characterizes the doublet system. The triplet has about the same distortion up to a half field angle of 10°, drops to zero at a field angle of 18°, and becomes barrel distortion beyond 18°. There is a noticeable degradation in the binocular performance of the triplet when compared with the doublet. However, there is no resulting loss of binocular fusion among any observers as might be expected. It appears that the design has been carried as far as possible and that further improvement in performance or increase in maximum field angle will probably require the addition of another element or the use of an aspheric surface.

Many questions have been left unanswered in this report. Further study is needed in the area of binocular vision in a biocular system. Two main areas of interest are magnification differences and limits on the relationship between

convergence and accommodation. Also, the question of the nonsymmetrical astigmatism and its effect on individual eyes needs further study.

Langley Research Center
National Aeronautics and Space Administration
Hampton, VA 23665
September 30, 1977

APPENDIX A

DEVELOPMENT OF AN ACHROMATIC DESIGN

The desired result in system performance is that all rays from a given point on the CRT emerge from the system on the observer's side as closely parallel to each other as possible. The basic design techniques consisted of reversing direction and tracing parallel rays from infinity on the observer's side back to the CRT surface and minimizing the aberrations in this plane. It is a relatively easy matter to relate the magnitude of these aberrations to the image distance and angular disparity curves previously mentioned.

The specific procedure used to accomplish the design closely follows the design method for a Taylor triplet type lens described in reference 5. However, a portion of the technique outlined there had to be modified to account for the fact that the entrance pupil was shifted from the middle lens of the triplet (an assumption made in ref. 5) to the observer plane which is located outside of the lens. The following sections will deal mainly with these modifications. Notice that because of the reversal of direction, the system exit pupil referred to in the main body of this report now becomes the system entrance pupil and vice versa. This definition will hold only in this appendix.

The procedure used in choosing the region of parameters to be investigated is outlined in figure 28. A target value of lateral chromatic aberration was chosen which resulted in reasonable lens powers for the system. The target value chosen was one-half that of the doublet system. Attempts to reduce this to a lower value resulted in lenses which were too powerful and hence too thick for the desired aperture diameters. Ranges of values of two parameters were chosen next. They were the ratio of the separation between the two lenses (R) and the field curvature (Petzval sum). Reference 5 gives a complete description of these two parameters. Each configuration of R and Petzval sum was analyzed by use of the first-order thin-lens analysis. This analysis resulted in a corresponding set of thin-lens powers and separations for each possible combination of R and Petzval sum. Each configuration of lens powers and separations was then analyzed by using the third-order thin-lens and third-order thick-lens analyses. The third-order thin-lens analysis provided a first iteration of the bending of each lens which will result in a desired state of monochromatic aberration correction. Bending is defined in terms of the first surface curvature of the lens. (See ref. 6.) Then, the third-order thick-lens analysis generated a set of individual surface curvatures and separations which corresponded to the lens powers and separations found in the third-order thin-lens analysis. Finally, the ray tracing was used to determine the combination of R, Petzval sum, and lens bendings which provides the optimum shape of the aberration curves over the entire field of view. Before describing these design steps in more detail, it is necessary to digress and look at the manner in which the ray tracing aberration curves are related to image distance and binocular disparity. In this way the optimum shape of the aberration curves can be specified which also will establish the target values of the aberrations to be used in the first- and third-order analyses.

APPENDIX A

Geometrical Ray Tracing

Parallel bundles of rays from infinity on the observer's side were traced through the system to their points of intersection with the CRT surface. Aberration curves were plotted showing the displacement on the CRT surface between the chief ray and each of the other rays as a function of the position of each incident ray in the entrance pupil. Figure 29 shows the geometrical arrangement of the input rays into the tangential and sagittal fans. The tangential fan consists of all rays lying in the ZY_{en} plane such as T_1, T_2, and the chief ray. The sagittal fan is defined by all rays, S_1, S_2, and the chief ray. The input rays are spaced along the X_{en} and Y_{en} axes from the center to the edge of the system entrance pupil. The diameter of the pupil represents the maximum allowable region of lateral and vertical eye displacement of the observer.

The aberration curves consist of plots of Y_T against Y_E and both Y_s and X_s against X_E. Since the tangential fan lies in a meridian plane of the system the plot of X_T against Y_E is identically zero. The following five equations relate the image distance to the slope of the different aberration curves and the binocular disparity to the amplitude of the different aberration curves. The general form of these relationships is derived in appendix B.

The slope of each aberration curve at a particular value of $X_E = X_{E1}$ and $Y_E = Y_{E1}$ may be related to one component (either tangential or sagittal) of the image distance for the eye of the observer at that position in the pupil.

At $Y_E = Y_{E1}$ and $X_E = 0$ (case A), the tangential image distance may be related to the slope of the tangential aberration curve dY_T/dY_E evaluated at $X_E = 0$ and $Y_E = Y_{E1}$ as

$$ID_{TA} = -\frac{f_L}{\left(\frac{dY_T}{dY_E}\right)_{\substack{X_E=0 \\ Y_E=Y_{E1}}}} + f_L - Z_o \qquad \text{(A1)}$$

where

f_L focal length of lens

Z_o distance from observer to primary principal plane of system

The sagittal image distance for case A may be related to the slope of the sagittal aberration dX_s/dX_E curve evaluated at $X_E = 0$, $Y_E = Y_{E1}$ as

$$ID_{SA} = -\frac{f_L}{\left(\frac{dX_s}{dX_E}\right)_{\substack{X_E=0 \\ Y_E=Y_{E1}}}} + f_L - Z_o \qquad \text{(A2)}$$

Evaluation of equation (A2) would require a separate sagittal ray trace for each value of Y_E to be used. Since the purpose of these equations is to provide an estimate and in the interest of economy, equation (A2) was not used and is presented here as information only.

Equations similar to equations (A1) and (A2) could be derived to estimate image distance in case B. This was not done because the image distance calculations and plots were not performed for case B. The general form of equations (A1) and (A2) is derived in appendix B.

The amplitude difference between two points of an aberration curve, the pupil coordinates of which correspond to the interocular distance, can be used to estimate the binocular disparity between chief rays passing through the center of each eye pupil. In case A the horizontal binocular disparity ΔU_{TA} is related to the distance between two points Y_{T2} and Y_{T1} on the curve of Y_T against Y_E as

$$\Delta U_{TA} = - \frac{Y_{T2} - Y_{T1}}{f_L - \left(\frac{f_L - Z_o}{2a}\right)(Y_{T2} - Y_{T1})} \tag{A3}$$

There is no vertical binocular disparity in case A since all chief rays through the eye pupils lie in the meridian plane of the system. In case B the horizontal disparity is related to the distance between two points X_{s2} and X_{s1} on the curve of X_s against X_E as

$$\Delta U_{SB} = - \frac{X_{s2} - X_{s1}}{f_L - \left(\frac{f_L - Z_o}{2a}\right)(X_{s2} - X_{s1})} \tag{A4}$$

In case B the vertical disparity (dipvergence) is related to the distance between two points Y_{s2} and Y_{s1} on the curve of Y_s against X_E as

$$\Delta U_{TB} = - \frac{Y_{s2} - Y_{s1}}{f_L - \left(\frac{f_L - Z_o}{2a}\right)(Y_{s2} - Y_{s1})} \tag{A5}$$

Equations (A3) and (A4) illustrate that the most uniform horizontal disparity over the allowable area of head displacement is achieved by reducing the difference between the Y_T and X_s aberration curves over the system entrance pupil. This difference is characteristic of astigmatism and is discussed later.

As an example of the application of the preceding idea, the plots of Y_T against Y_E and X_s against X_{E1} for the triplet are shown in figures 30 and 31. Figure 30 treats the case of zero field angle and figure 31 treats the

case of a 10° half field angle. The axial point on the CRT is located 7.95 cm inside of the paraxial focus. The appropriate equations described in the previous paragraph can be used to relate these curves to the respective image distances and binocular disparities. As an example for zero field angle, the slope of the Y_T against Y_E curve is 0.13. Substituting this value into equation (A1) with f_L = 61 cm and Z_o = 76.2 cm results in an image distance of -4.85 m which agrees closely with the value of 4.91 m taken from figure 18. The sign difference is due to the reversal of direction between the ray tracing of figure 18 and equation (A1). Also from figure 30, the $(Y_{T2} - Y_{T1})$ value corresponding to $Y_{E2} - Y_{E1}$ = 6.35 cm with both eyes equally spaced on either side of the optic axis is

$$Y_{T2} - Y_{T1} = 0.78 \text{ cm}$$

Substituting this equation into equation (A5) results in a horizontal disparity of

$$\Delta U_{TA} = -42.6 \text{ arc minutes}$$

which agrees closely with the value of 43 arc minutes from figure 20. The sign reversal is due to the reversal of direction of the ray tracing between figure 20 and equation (A3).

As mentioned in appendix B, the desirable slope of the aberration curve is positive with a value between 0 and 1. As shown in the previous example, a slope of 0.13 will provide a virtual image at about 5 m.

The shape of the curves at zero field angle is typical of spherical aberration whereas at a finite field angle it is typical of coma. This statement is especially true in the region of negative slope. Also the difference between Y_T and X_S at the finite field angle is typical of astigmatism. The spherical aberration and coma will cause a nonuniformity of collimation along either the X or Y axis in the system aperture. Astigmatism over the system entrance pupil will cause a difference of binocular disparity for horizontal and vertical head displacements as previously mentioned. Therefore, the design goal has been a reduction of all three of these aberrations. Because a reduction of coma brought about an increase in distortion at higher field angles, a trade-off was made between the two which turned out to be close to the point of minimum astigmatism.

Details of Design Procedure

First-order thin-lens analysis.- The classical technique was used here to determine the lens powers and separations which would provide a desired state of color correction and Petzval curvature, and was performed for values of R ranging from 0.65 to 0.95 and values of Petzval sum ranging from -0.0319 to -0.0327.

APPENDIX A

The method outlined in reference 5 is based on the assumption that the aperture is located coincident with the middle lens of the system. Since the aperture stop of the system under study is located in front of the first lens, the first question to be answered was the determination of the effect of the aperture shift on the results of the first-order analysis. Longitudinal chromatic aberration (focal shift) is independent of aperture position. Lateral chromatic aberration is dependent on aperture position but the values predicted by the classical first-order analysis were affected very little by the aperture shift. Specifically, the first-order analysis predicted a 50-percent reduction in lateral chromatic aberration of the triplet system relative to the doublet system and this result was later verified in the ray tracing.

Third-order thin-lens analysis.- From reference 5, the third-order thin-lens approximation of the Seidel coefficients: spherical, coma, astigmatism, and distortion, may be written as

$$\left.\begin{aligned} \Sigma B &= B_1^{\bullet} + B_2^{\bullet} + B_3^{\bullet} && \text{(Spherical)} \\ \Sigma F &= F_1^{\bullet} + F_2^{\bullet} + F_3^{\bullet} && \text{(Coma)} \\ \Sigma C &= C_1^{\bullet} + C_2^{\bullet} + C_3^{\bullet} && \text{(Astigmatism)} \\ \Sigma E &= E_1^{\bullet} + E_2^{\bullet} + E_3^{\bullet} && \text{(Distortion)} \end{aligned}\right\} \tag{A6}$$

In these equations the subscripts 1, 2, and 3 refer to the aberration contribution of each lens. The individual contributions of each lens to each aberration have the form

$$\left.\begin{aligned} B_1^{\bullet} &= \alpha_{11}^{\bullet} + \alpha_{21}^{\bullet} C_2 + \alpha_{31}^{\bullet} C_2^2 \\ B_2^{\bullet} &= \alpha_{12}^{\bullet} + \alpha_{22}^{\bullet} C_4 + \alpha_{32}^{\bullet} C_4^2 \\ B_3^{\bullet} &= \alpha_{13}^{\bullet} + \alpha_{23}^{\bullet} C_6 + \alpha_{33}^{\bullet} C_6^2 \\ F_1^{\bullet} &= \beta_{11}^{\bullet} + \beta_{21}^{\bullet} C_2 + \beta_{31}^{\bullet} C_2^2 \\ F_2^{\bullet} &= \beta_{12}^{\bullet} + \beta_{22}^{\bullet} C_4 + \beta_{32}^{\bullet} C_4^2 \\ F_3^{\bullet} &= \beta_{13}^{\bullet} + \beta_{23}^{\bullet} C_6 + \beta_{33}^{\bullet} C_6^2 \\ C_1^{\bullet} &= \gamma_{11}^{\bullet} + \gamma_{21}^{\bullet} C_2 + \gamma_{31}^{\bullet} C_2^2 \\ C_2^{\bullet} &= \gamma_{12}^{\bullet} + \gamma_{22}^{\bullet} C_4 + \gamma_{32}^{\bullet} C_4^2 \\ C_3^{\bullet} &= \gamma_{13}^{\bullet} + \gamma_{23}^{\bullet} C_6 + \gamma_{33}^{\bullet} C_6^2 \\ E_1^{\bullet} &= \delta_{11}^{\bullet} + \delta_{21}^{\bullet} C_2 + \delta_{31}^{\bullet} C_2^2 \\ E_2^{\bullet} &= \delta_{12}^{\bullet} + \delta_{22}^{\bullet} C_4 + \delta_{32}^{\bullet} C_4^2 \\ E_3^{\bullet} &= \delta_{13}^{\bullet} + \delta_{23}^{\bullet} C_6 + \delta_{33}^{\bullet} C_6^2 \end{aligned}\right\} \tag{A7}$$

APPENDIX A

The $\alpha_{ij}^{\bullet}$, $\beta_{ij}^{\bullet}$, $\gamma_{ij}^{\bullet}$, and $\delta_{ij}^{\bullet}$ terms are determined from the first-order thin-lens ray trace. The terms C_2, C_4, and C_6 are the first surface curvatures of the first, second, and third lenses, respectively. Substitution of equations (A7) into equations (A6) results in the set of equations which must be solved.

An example of the use of these equations in the design of a triplet is given in reference 5. In the example, the chief ray passes through the center of lens 2 (assumed to be the aperture) which causes many of the terms in equations (A7) to go to zero. This simplifying assumption cannot be made in the case being studied here because the aperture is outside the system. Therefore, all terms in equations (A6) have finite value and it becomes a case of solving four quadratic equations in three unknowns. A graphical method was used in the solution of this problem. Plots of $B_1^{\bullet}$, $B_2^{\bullet}$, and $B_3^{\bullet}$ were made as shown in figure 32. Each of these functions is plotted as a function of the first surface curvature of the three respective lenses. The curves for $B_1^{\bullet}$ and $B_3^{\bullet}$, the two positive lenses, are concave downward while $B_2^{\bullet}$ is concave upward. Similar curves may be drawn for the other three Seidel aberrations as shown in figures 33 to 35. Theoretically, any one of the aberrations could be reduced to zero by choosing the values of C_2 and C_6 to give peak values to the aberration of the positive lens such as points $B_{1,max}^{\bullet}$ and $B_{3,max}^{\bullet}$ in figure 32. Then by choosing C_4 to give

$$B_2^{\bullet} = -(B_{1,max}^{\bullet} + B_{3,max}^{\bullet}).$$

the total aberration ΣB will be zero. This procedure could be repeated for ΣF, ΣC, or ΣE. It is impossible to find a set of first surface curvatures to satisfy the target values specified in reference 5. These values are

$$\Sigma B = 0$$

$$\Sigma F = 0$$

$$\Sigma C = -1/3(P_C \Phi^2)$$

$$\Sigma E = 0$$

Therefore, a trade-off must be made between the four aberrations to give the most desirable shape to the aberration curves. Also the higher order aberrations place a limit on the magnitude of any aberration cancellation performed by lens 2; thus, it is impossible to exactly cancel even one of the aberrations in equation (A1). Instead a minimum is found by means of trial and error.

Third-order thick-lens analysis.- The finite lens thickness and second surface curvature are now added to maintain the thick-lens power equal to the thin-lens power (ref. 7). Also, surface separations t_b and t_d in figure 23 are set so that the separation between principal planes of the individual thick lenses equals the thin-lens separations determined in the first-order analysis.

Application of procedure.- The methods described were used to determine the aberration curves for spherical, coma, astigmatism, and distortion for a number of configurations of lens powers and separations determined in the

first-order analysis. The third-order thin-lens curves were first plotted for values of R ranging from 0.65 to 0.95. The minimum magnitudes of coma, astigmatism, and distortion for each R value occurred for different bendings of the individual lenses. For each value of R, a bending of each lens was chosen which was halfway between the minimum coma and minimum distortion of the total system. This condition occurred approximately at the condition of peak astigmatism of lenses 1 and 3 resulting in a minimum system astigmatism. The configuration of surface curvatures and separations for each value of R in the region of interest were then ray traced. An optimum value of R was chosen on the basis of minimum coma like appearance, minimum separation of the tangential and sagittal aberration curves, and minimum distortion at all field angles. The need for minimum difference between tangential and sagittal aberration curves was discussed earlier in this appendix. The final value of R was chosen at 0.75. This procedure was repeated by holding R constant and varying the Petzval sum, the optimum Petzval curvature being found to be -0.0319. As a final step, the bending of each lens was varied about the point obtained from the steps outlined. The final configuration of lens curvatures and separations is shown in table I. All the variations of system parameters were subject to three constraints: (1) the edge thickness geometry of lenses 1 and 3, (2) the edge clearance geometry between lenses 2 and 3, and (3) total internal reflection which was encountered at the second surface of lens 2 at large field angles.

It appears that the design has been carried as far as possible and that further improvement in performance or increase in maximum field angle will probably require the addition of another element or the use of an aspheric surface.

APPENDIX B

RELATIONSHIP OF ABERRATION CURVES TO IMAGE DISTANCE

This appendix describes a method by which the classical aberration curves plotted in the plane of the CRT for the condition of parallel light rays traced from the observer's side to the CRT may be used to predict the behavior of the apparent image distance when the observer views the CRT through the lens. As a result, it is possible to determine the shape of the aberration curve which will provide the most desirable image distance performance over the field of view and range of allowable head displacement.

By way of introduction, it is necessary to explain the concept of object and image space. (See ref. 8.) Any point of object space is said to be conjugate to a single point in image space and vice versa. For a thin lens, this conjugate relationship is specified by

$$\frac{1}{s} + \frac{1}{s'} = \frac{1}{f_L} \tag{B1}$$

where

s distance measured from object to lens

s' distance measured from lens to image

f_L focal length of lens

The sign convention used is that all distances are measured positive from left to right.

Figure 36 illustrates the geometry involved in equation (B1). The same equations hold for a thick lens except that s and s' are measured relative to the principal planes of the system. The observer is located in image space and the CRT is in object space. By using the same sign convention, the image distance ID_{av} is defined as the distance from the observer to the image

$$ID_{av} = s' - Z_o \tag{B2}$$

A virtual image ($s' < 0$) will always result in a negative value of ID. In image space, parallel light corresponds to an infinite image distance ($s' = \infty$), diverging light corresponds to a finite distant virtual image ($s' < 0$), and converging light corresponds to a real image ($s' > 0$).

The ray tracing proceeds from image space to object space. The rays in image space are parallel ($s_1' = \infty$) at a height Δr above the axis, whereas the rays in object space converge to a focus ($s_1 = f_L$). This is illustrated in figure 37(a). The question to be answered is what will be the behavior of rays in image space when the object is displaced from the focal point f_L by the distance t_{K1} or t_{K2} in the figure.

APPENDIX B

If the object space point is displaced from f_L to O_2, outside of the focal point, a real image is formed at I_2 and the conjugate object distance is defined as (see figs. 37(a) and 37(b))

$$s_2 = f_L + t_{K1} \tag{B3}$$

From equation (B1)

$$s_2' = \frac{f_L s_2}{s_2 - f_L} \tag{B4}$$

Substituting equation (B3) into equation (B4) and simplifying results in

$$s_2' = \frac{f_L^2}{t_{K1}} + f_L \tag{B5}$$

To determine the relationship between t_{K1} and the slope of the aberration curve da/dr, the following geometrical relationship is seen in figure 37(a):

$$\frac{-\Delta a_2}{t_{K1}} = \frac{\Delta r}{f_L} \tag{B6}$$

The negative value comes from the fact that positive quantities are measured upward. This equation may be written as

$$t_{K1} = -f_L \frac{\Delta a}{\Delta r} \tag{B7}$$

Taking the limit of small Δr yields

$$t_{K1} = -f_L \frac{da}{dr} \tag{B8}$$

Substituting equation (B8) into equation (B5) gives

$$s_2' = -\frac{f_L}{da/dr} + f_L \tag{B9}$$

Substituting equation (B9) into equation (B2) yields

$$ID_{av} = -\frac{f_L}{da/dr} + f_L - Z_o \tag{B10}$$

Similarly, if the object space point is displaced by t_{K2} to a point O_2 inside the focal point, a virtual image is formed at I_3 and the conjugate object distance is (see figs. 37(a) and 37(c))

$$s_3 = f_L - t_{K2} \tag{B11}$$

From equation (B1)

$$s_3' = \frac{f_L s_3}{s_3 - f_L} \tag{B12}$$

Substituting equation (B11) into equation (B12) and simplifying results in

$$s_3' = - \frac{f_L^2}{t_{K2}} + f_L \tag{B13}$$

Referring again to figure 37(a) with the object point at O_3 yields

$$\frac{\Delta a_3}{t_{K2}} = \frac{\Delta r}{f_L} \tag{B14}$$

and again taking this relationship to the limit of small Δr yields

$$t_{K2} = + f_L \frac{da}{dr} \tag{B15}$$

Substituting equation (B15) into equation (B13) yields

$$s_3' = - \frac{f_L}{da/dr} + f_L \tag{B16}$$

Finally, by substituting equation (B16) into equation (B2),

$$ID_{av} = - \frac{f_L}{da/dr} + f_L - Z_o \tag{B17}$$

Equations (B17) and (B10) are identical and provide the desired relationship between ID_{av} and da/dr for any point in object space.

Equation (B17) is only valid for 0^o half field angle. At finite field angles there are two separate focal points, one for the tangential and one for the sagittal rays. Also the term f_L in the equations is modified by an obliquity factor as described by the Coddington equations. (See ref. 9.) This obliquity factor is a constant for a given field angle. Therefore, the sagittal and tangential image distances (referred to in the main body of the paper)

each have a relationship to the slopes of the sagittal and tangential aberration curves, respectively.

Several characteristics of equation (B17) are worth noting.

(1) If $\frac{da}{dr} = 0$, then $ID_{av} = -\infty$.

(2) If $\frac{da}{dr} = +1$, then $ID_{av} = -Z_o$.

(3) If $\frac{da}{dr} = -1$, then $ID_{av} = 2f_L - Z_o$.

A virtual image will exist for $-Z_o > ID_{av} > -\infty$; therefore, virtual images are obtained over the range

$$0 < \frac{da}{dr} < 1 \tag{B18}$$

The relationship between the amplitude of the aberration curve Δa and the binocular disparity ΔU can be derived in a fashion similar to that described. By referring to figure 38, ΔU is related to ID_{av} as

$$\Delta U = \frac{2a}{ID_{av}} \tag{B19}$$

Substituting equations (B2) and (B5) into equation (B19) yields

$$\Delta U = \frac{2a}{\frac{f_L^2}{t_{K1}} + f_L - Z_o} \tag{B20}$$

Substituting equation (B7) into equation (B20) yields

$$\Delta U = \frac{2a}{\frac{f_L}{-\Delta a/\Delta r} + f_L - Z_o} \tag{B21}$$

By simplifying,

$$\Delta U = - \frac{2a \frac{\Delta a}{\Delta r}}{f_L - (f_L - Z_o)\frac{\Delta a}{\Delta r}} \tag{B22}$$

Now from the figure $\Delta r = 2a$

$$\Delta U = - \frac{\Delta a}{f_L - \frac{f_L - Z_o}{2a} \Delta a} \tag{B23}$$

A virtual image corresponds to diverging light and since the value of ID_{av} is negative for a virtual image, equation (B19) dictates a negative value of ΔU for diverging light.

Using equations (B13) and (B14) in place of equations (B5) and (B7) (this would be the case of a virtual image) results in an equation which is identical to equation (B23). Therefore, for any point in image space, equation (B23) provides the relationship between the amplitude of the aberration curve and binocular disparity.

The use of equations (B17), (B18), and (B23) provides a reasonably accurate prediction of image distance over the system exit pupil based on the aberration curve data. These data can be generated more easily and economically than the complete image distance data described in the main body of this report. It is an economical and easily used design tool but is not meant to replace the complete image distance calculations which are more accurate and show the effect of astigmatism more readily.

REFERENCES

1. Brewer, Silas: POLYPAGOS: Polychromic Program for the Analysis of General Optical Systems. SAMSO-TR-70-411, U.S. Air Force, Sept. 1970. (Available from DDC as AD 715 262.)

2. Ganzler, Bruce C.: Virtual Image Display for Flight Simulation. NASA TM X-2327, 1971.

3. Borish, Irvin M.: Clinical Refraction. Third ed., Professional Press, Inc., 1975.

4. Ogle, Kenneth N.: Researches in Binocular Vision. Hafner Publ. Co., 1964.

5. Military Standardization Handbook - Optical Design. MIL-HDBK-141, Oct. 5, 1962.

6. Conrady, A. E.: Applied Optics and Optical Design. Dover Publ., Inc., c.1957.

7. Stephens, Robert E.: The Design of Triplet Anastigmat Lenses of the Taylor Type. J. Opt. Soc. America, vol. 38, no. 12, Dec. 1948, pp. 1032-1039.

8. Hardy, Arthur C.; and Perrin, Fred H.: The Principles of Optics. McGraw-Hill Book Co., Inc., 1932.

9. Strong, John: Concepts of Classical Optics. W. H. Freeman and Co., 1958.

TABLE I.- PARAMETERS OF TRIPLET f_L = 61 cm

Surface	Surface curvature, ρ_i, 1/cm	Index of refraction at 5200 Å	Radius of clear aperture, cm
1	8.858×10^{-3}	1.4936	25.4
2	-15.709	1.0	25.4
3	5.512	1.5992	25.4
4	27.001	1.0	25.4
5	21.260	1.4936	25.4
6	-16.968	1.0	25.4

Separation	Separation, t_i, cm
a	9.445
b	4.156
c	3.810
d	2.666
e	16.247
f	39.450

TABLE II.- MAXIMUM ASTIGMATISM IN DIOPTERS FOR A MAXIMUM EYE DISPLACEMENT OF $\pm$6 cm

System	Maximum astigmatism, diopters, for half field angles, deg, of -			
	0	5	10	15
Triplet	0.037	0.105	0.195	0.092
Doublet	.023	.035	.050	.075

TABLE III.- MAXIMUM HORIZONTAL DISPARITY IN ARC MINUTES

(a) Case A

System	Maximum horizontal disparity, arc min, for half field angle, deg, of -			
	0	5	10	15
Triplet	+42.0	+42.0	+37.0	+31.0
Doublet	+44.0	+42.0	+40.0	+32.0

(b) Case B

System	Maximum horizontal disparity, arc min, for half field angle, deg, of -			
	0	5	10	15
Triplet	+42.0	+40.0	+32.0	+20.0
Doublet	+44.0	+42.0	+38.0	+27.0

TABLE IV.- MAXIMUM VERTICAL DISPARITY IN ARC MINUTES

(a) Case A

System	Maximum vertical disparity, arc min, for half field angle, deg, of -			
	0	5	10	15
Triplet	0	0	0	0
Doublet	0	0	0	0

(b) Case B

System	Maximum vertical disparity, arc min, for half field angle, deg, of -			
	0	5	10	15
Triplet	0	3.0	5.0	7.0
Doublet	0	.5	.5	1.0

TABLE V.- MAXIMUM PERCENT MAGNIFICATION DIFFERENCES BETWEEN THE TWO EYES FOR A MAXIMUM HEAD MOTION OF $\pm$3.0 cm

(a) Case A

System	Magnification differences between two eyes, percent, for half field angle, deg, of -			
	0	5	10	15
Triplet	2.55	5.55	6.17	15.10
Doublet	.83	1.26	1.86	3.00

(b) Case B

System	Magnification differences between two eyes, for half field angle, deg, of -			
	0	5	10	15
Triplet	0.3	4.1	1.1	1.36
Doublet	.15	2.5	1.15	.69

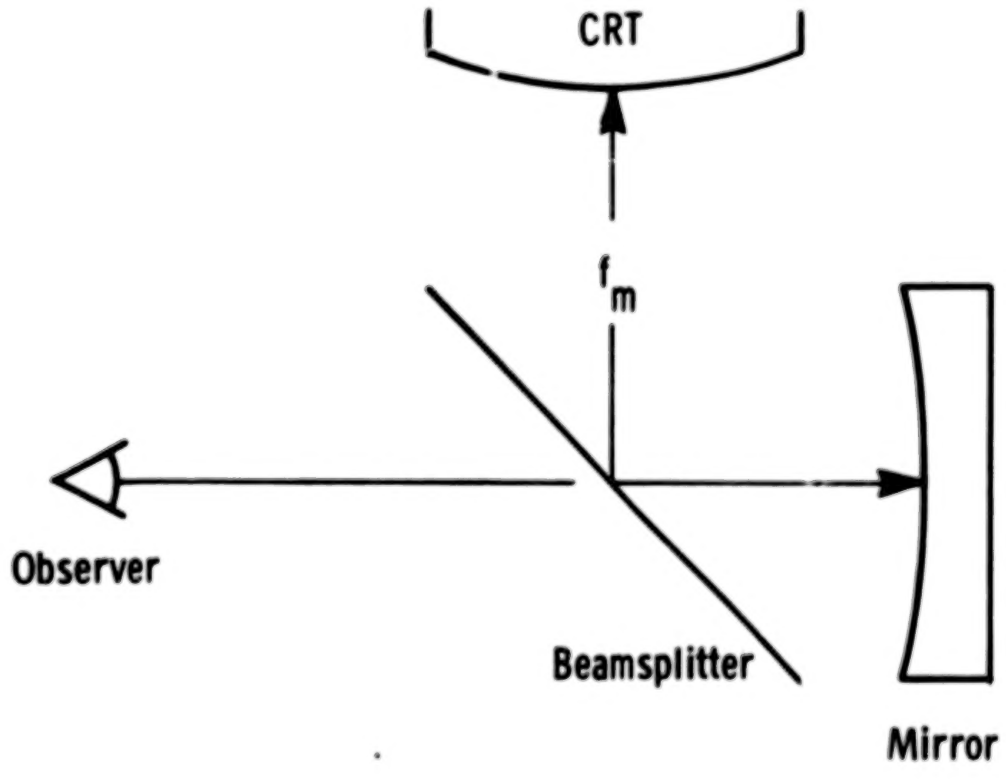

Reflective type

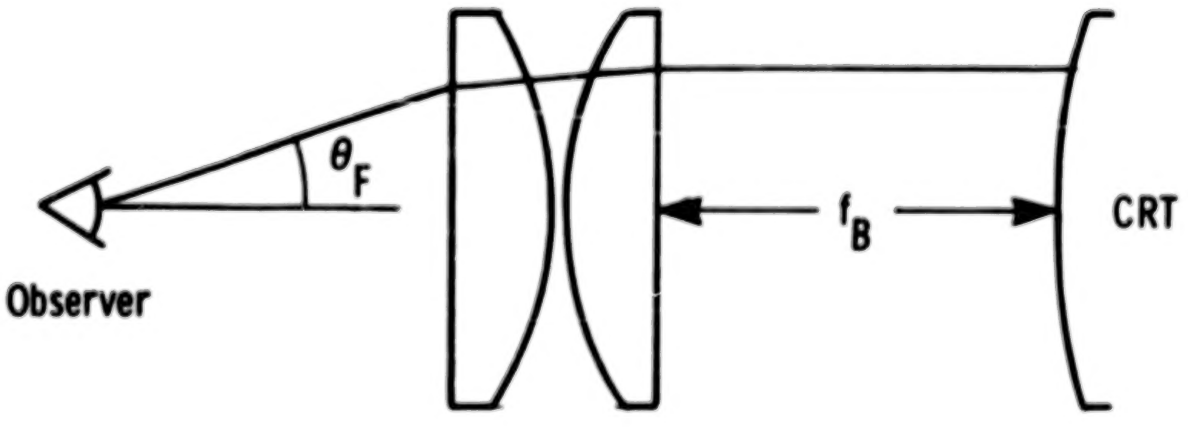

Refractive doublet

Figure 1.- Virtual image systems.

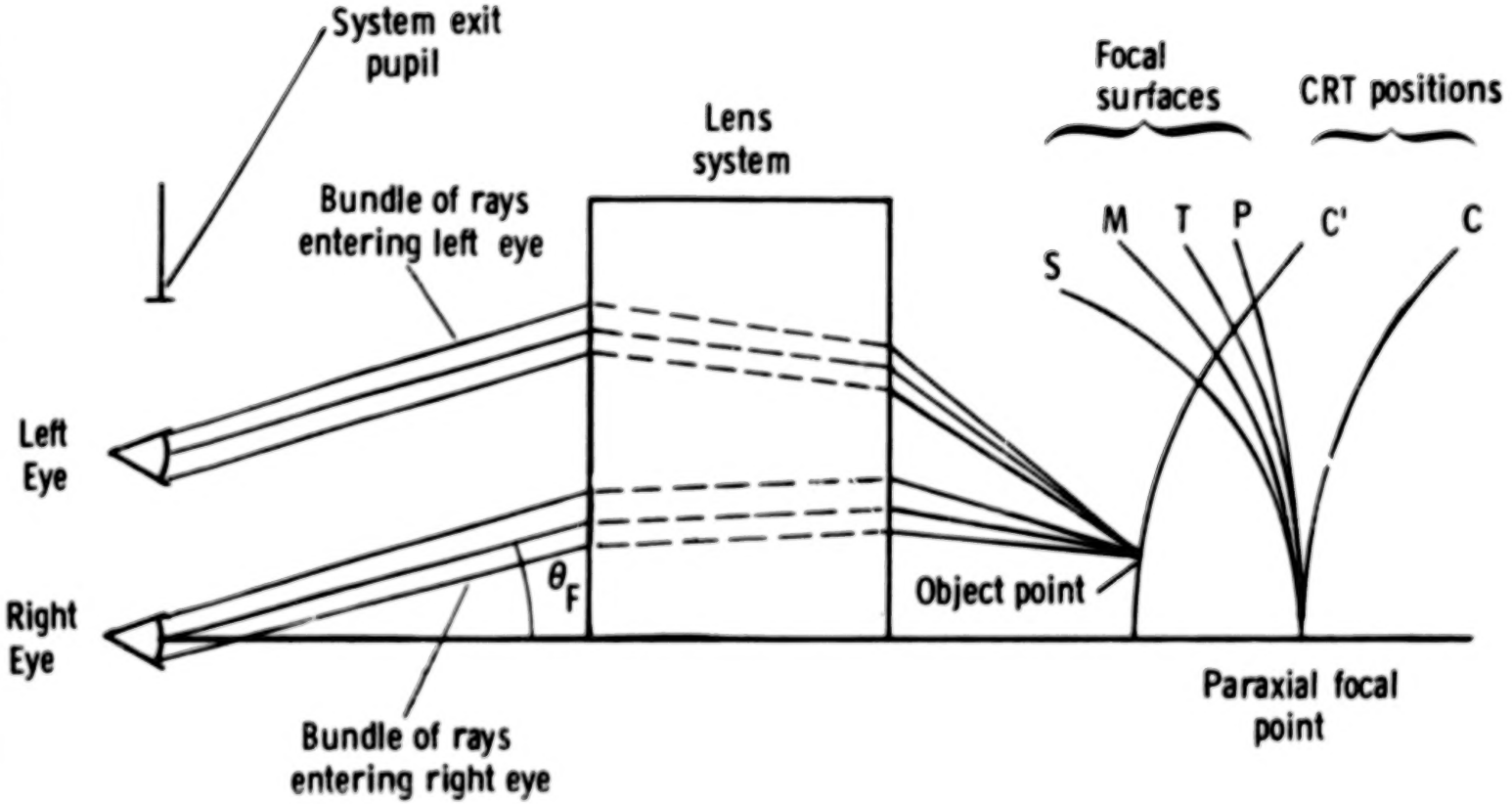

Figure 2.- Relationship between CRT positions and focal surfaces.

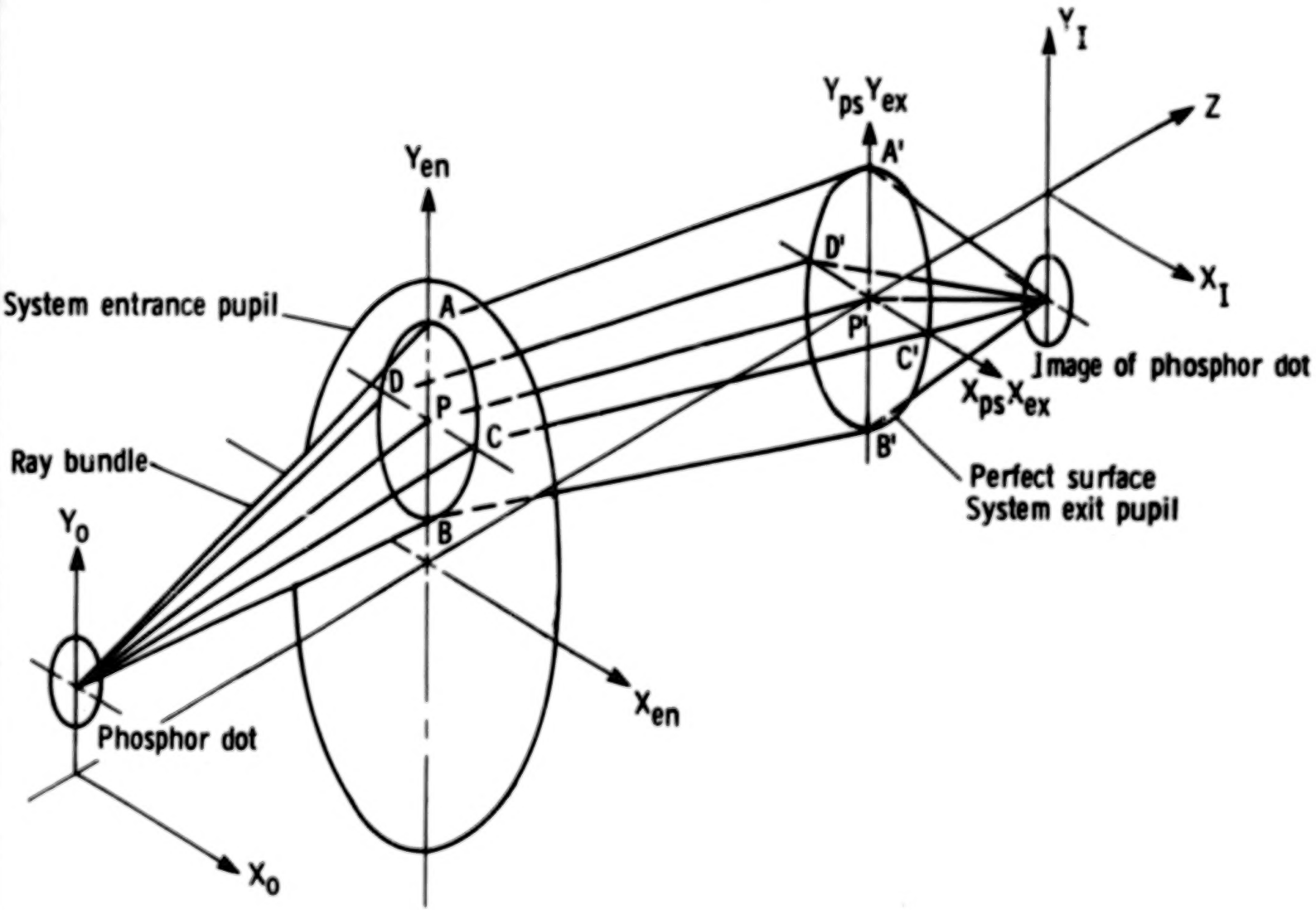

Figure 3.- Dot ray tracing geometry.

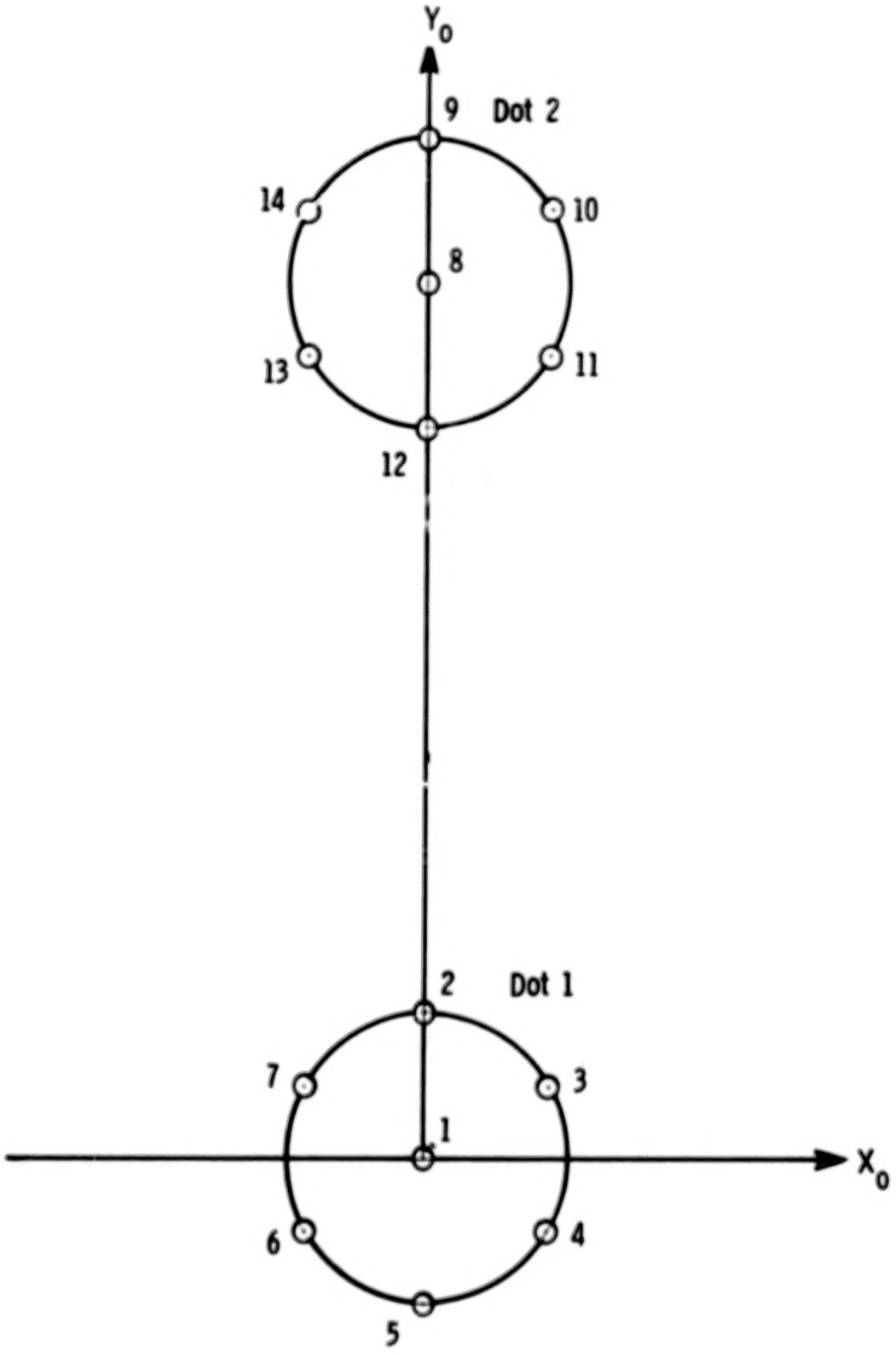

Figure 4.- Origin points of ray bundles on two adjacent like-color dots.

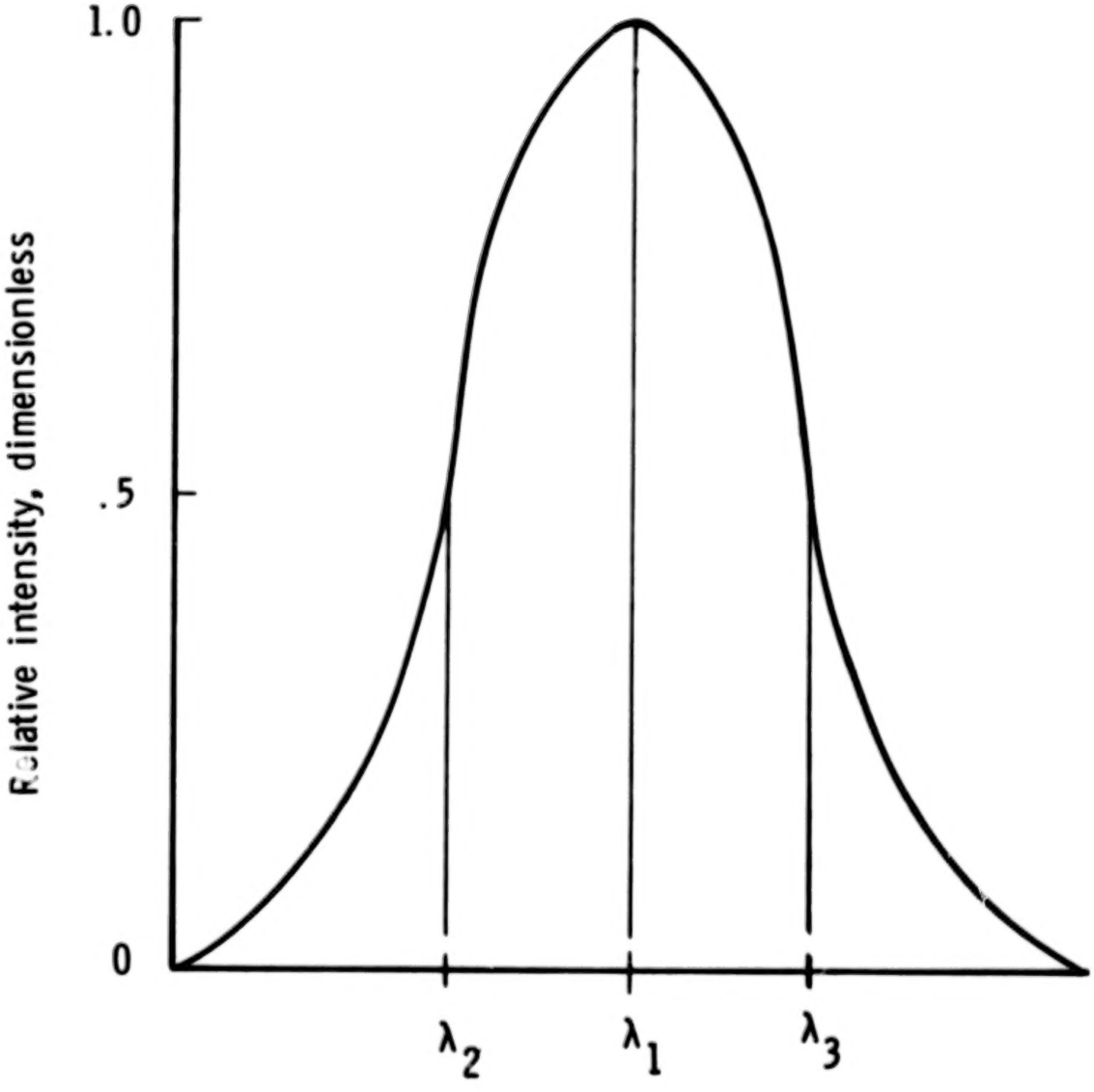

Figure 5.- Relative intensity of CRT phosphor as a function of wavelength.

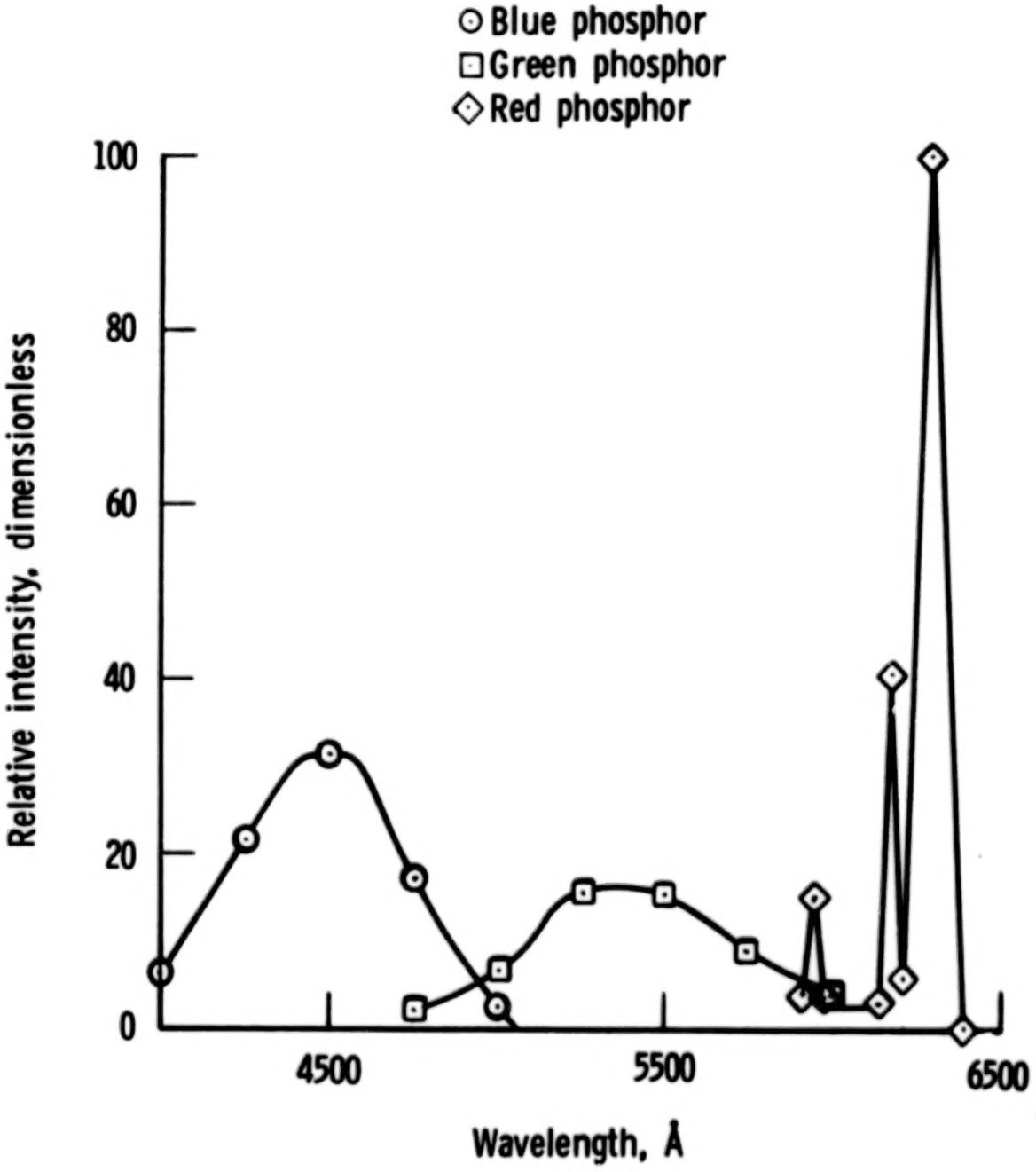

Figure 6.- Spectral output of color CRT.

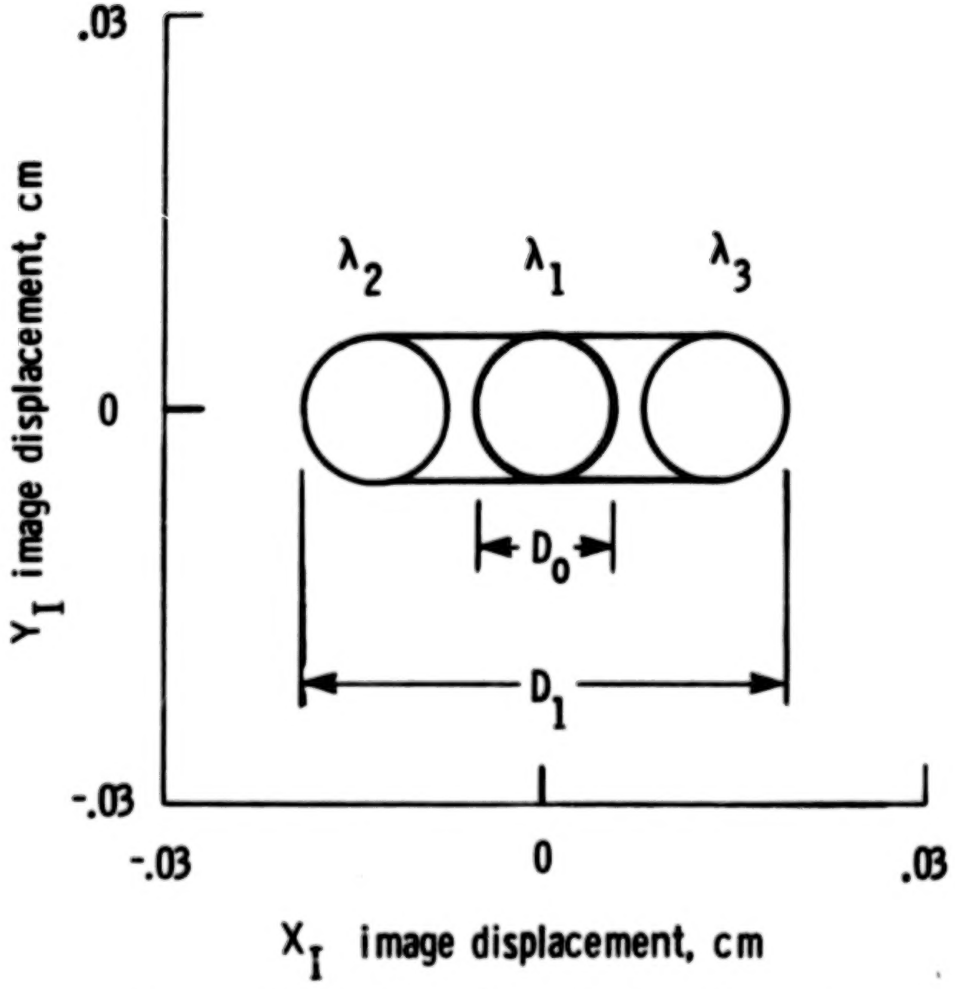

Figure 7.- Typical dot image showing elongation.

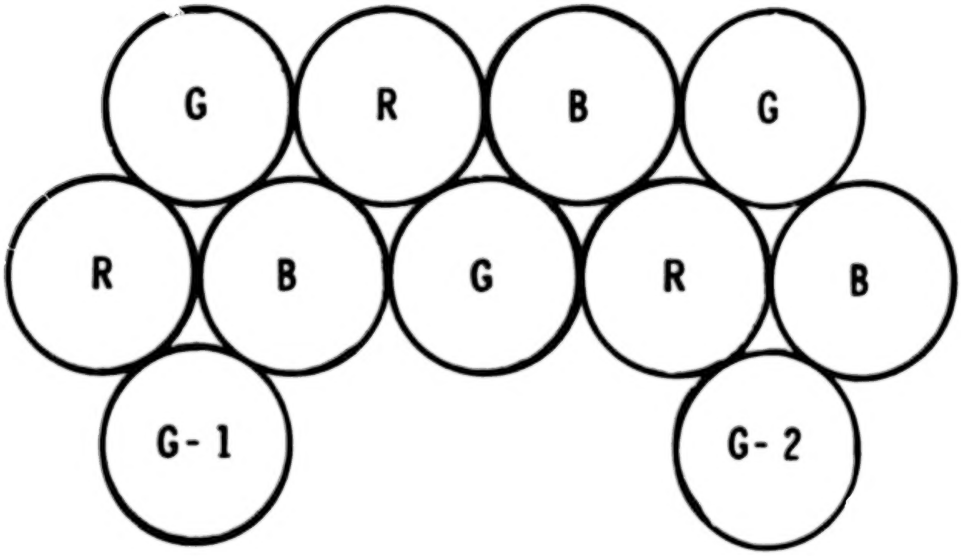

(a) CRT phosphor dot pattern.

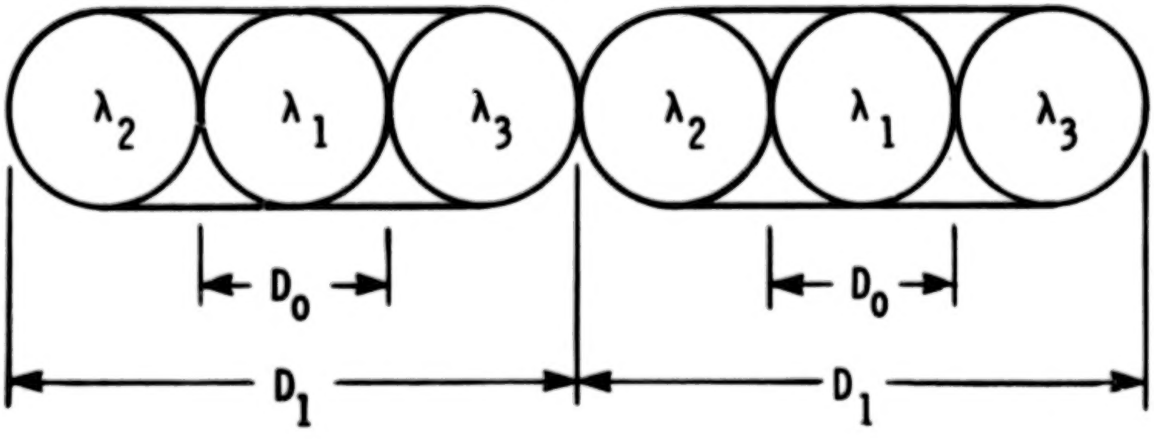

(b) Chromatically aberrated dot images.

Figure 8.- Details of CRT dot patterns.

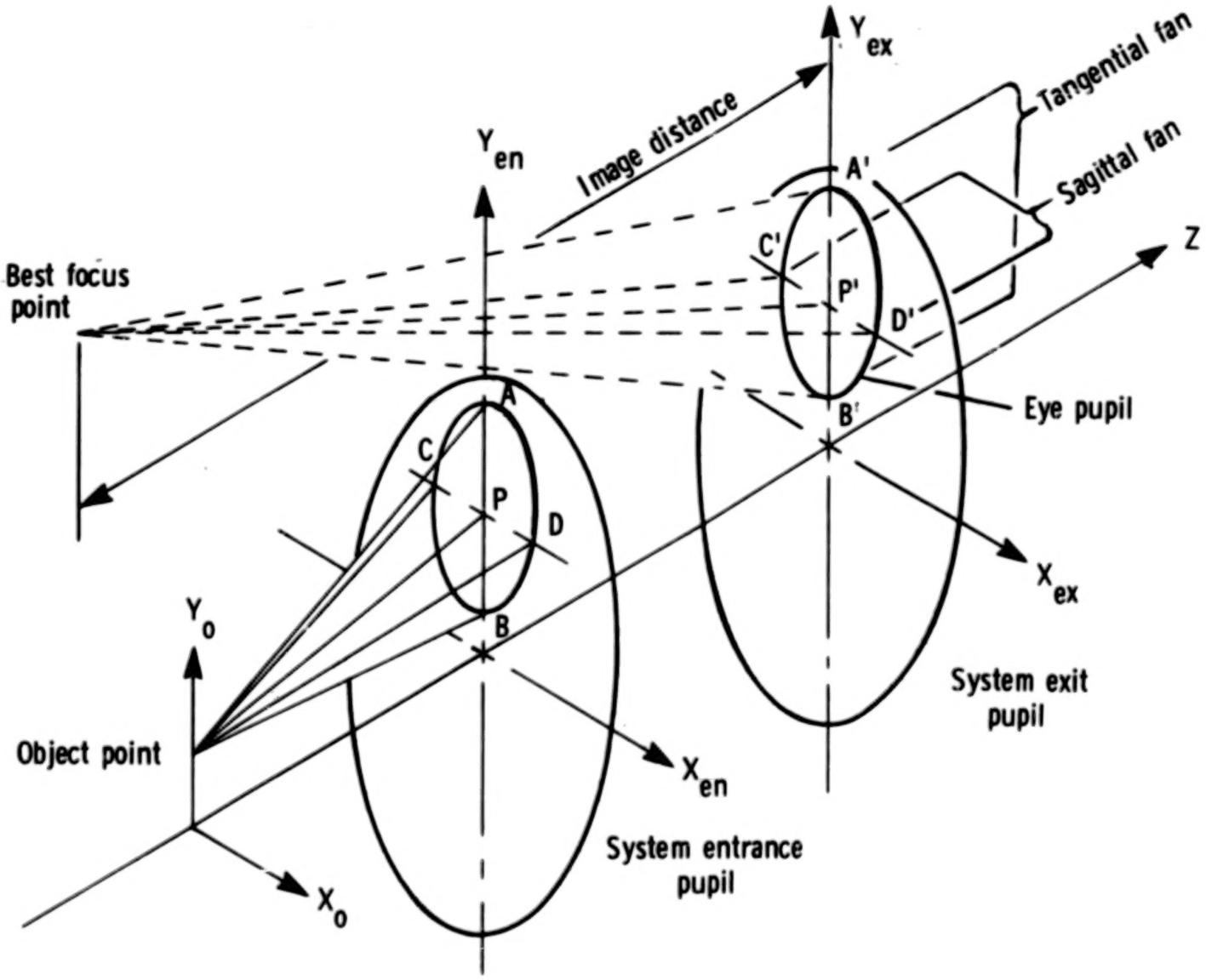

Figure 9.- Ray bundle configuration used in image distance and astigmatism calculations.

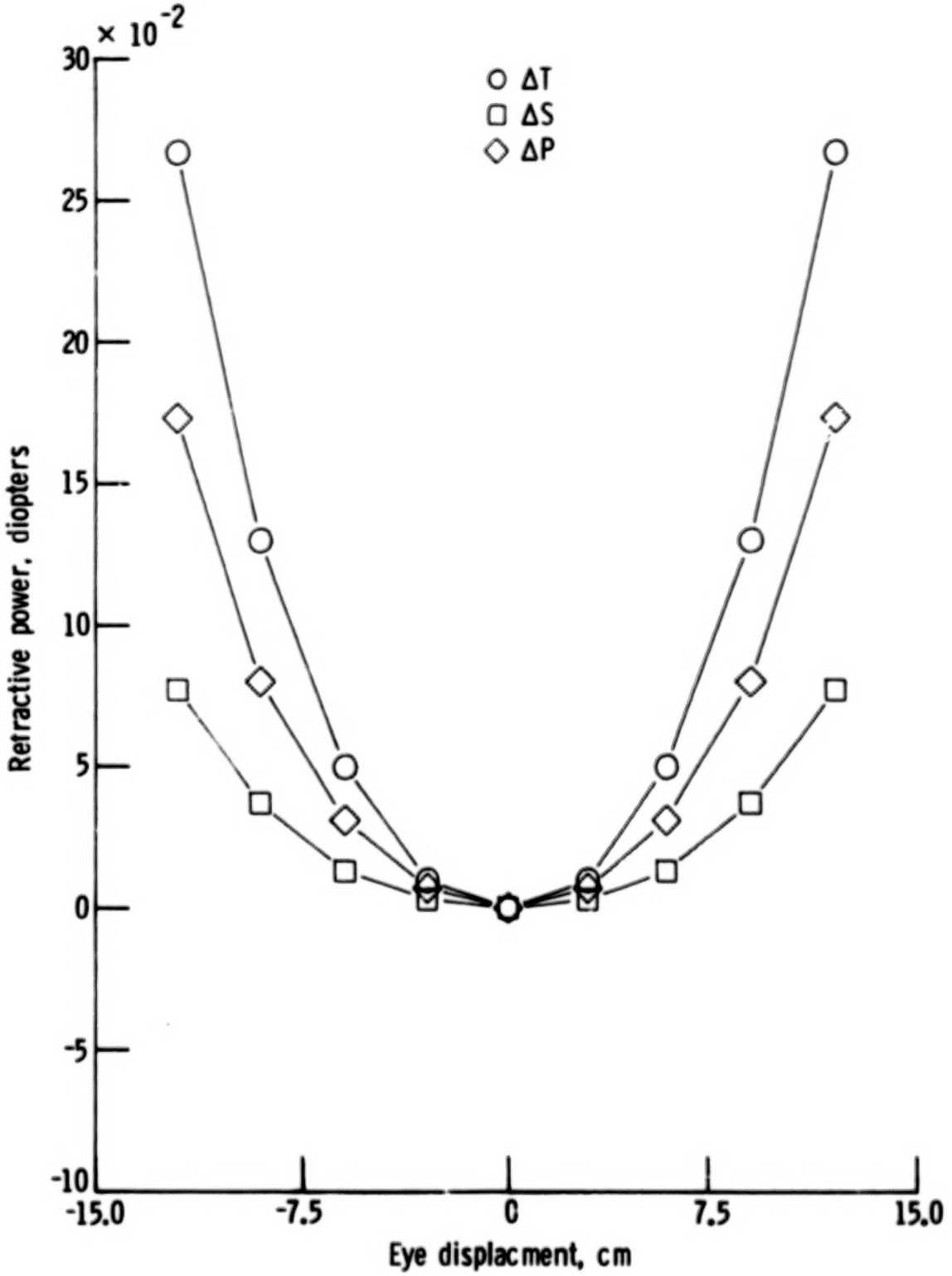

Figure 10.- Typical plot of ΔT, ΔS, and ΔP.

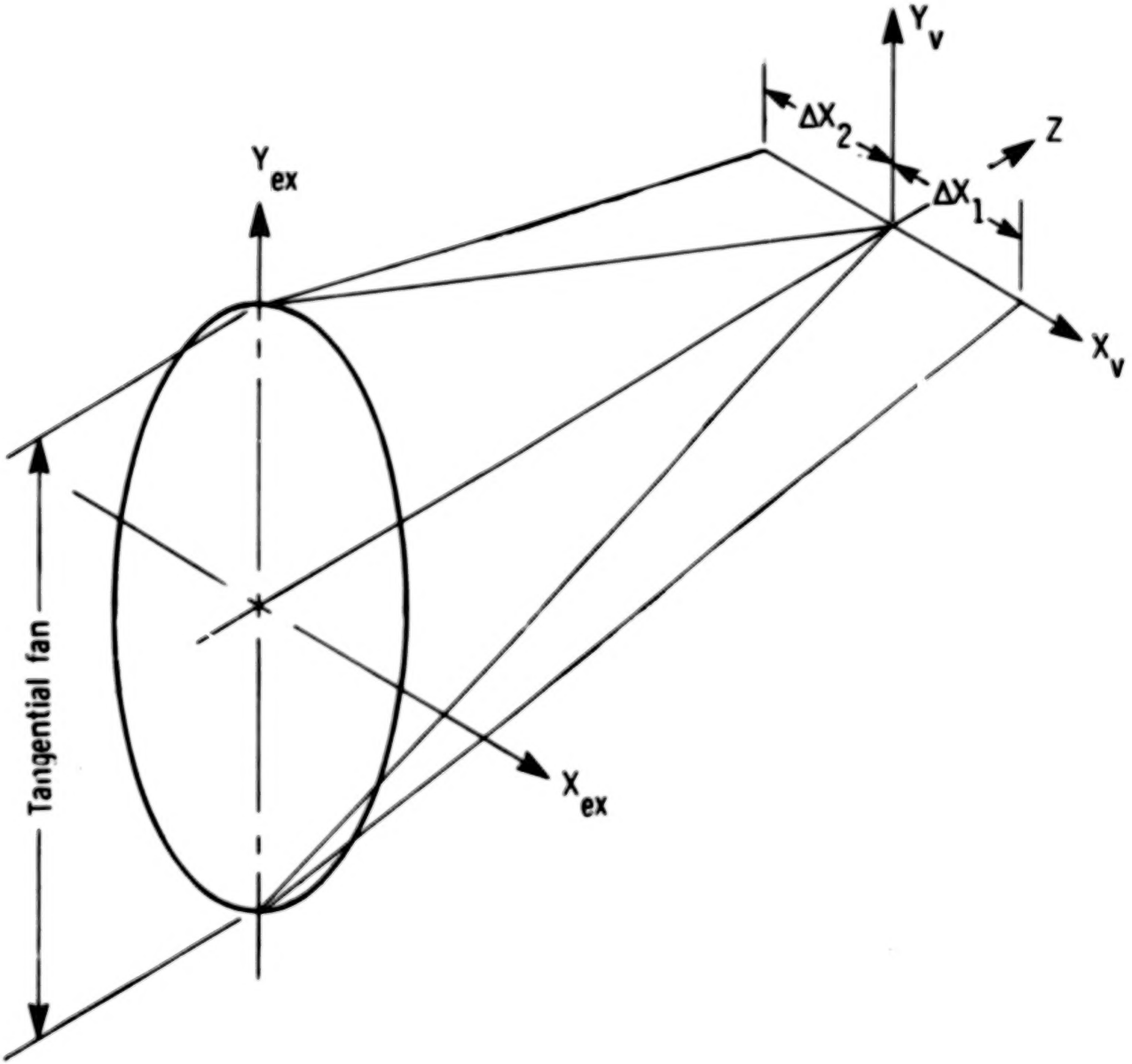

Figure 11.- Geometry of actual ray paths of tangential fan.

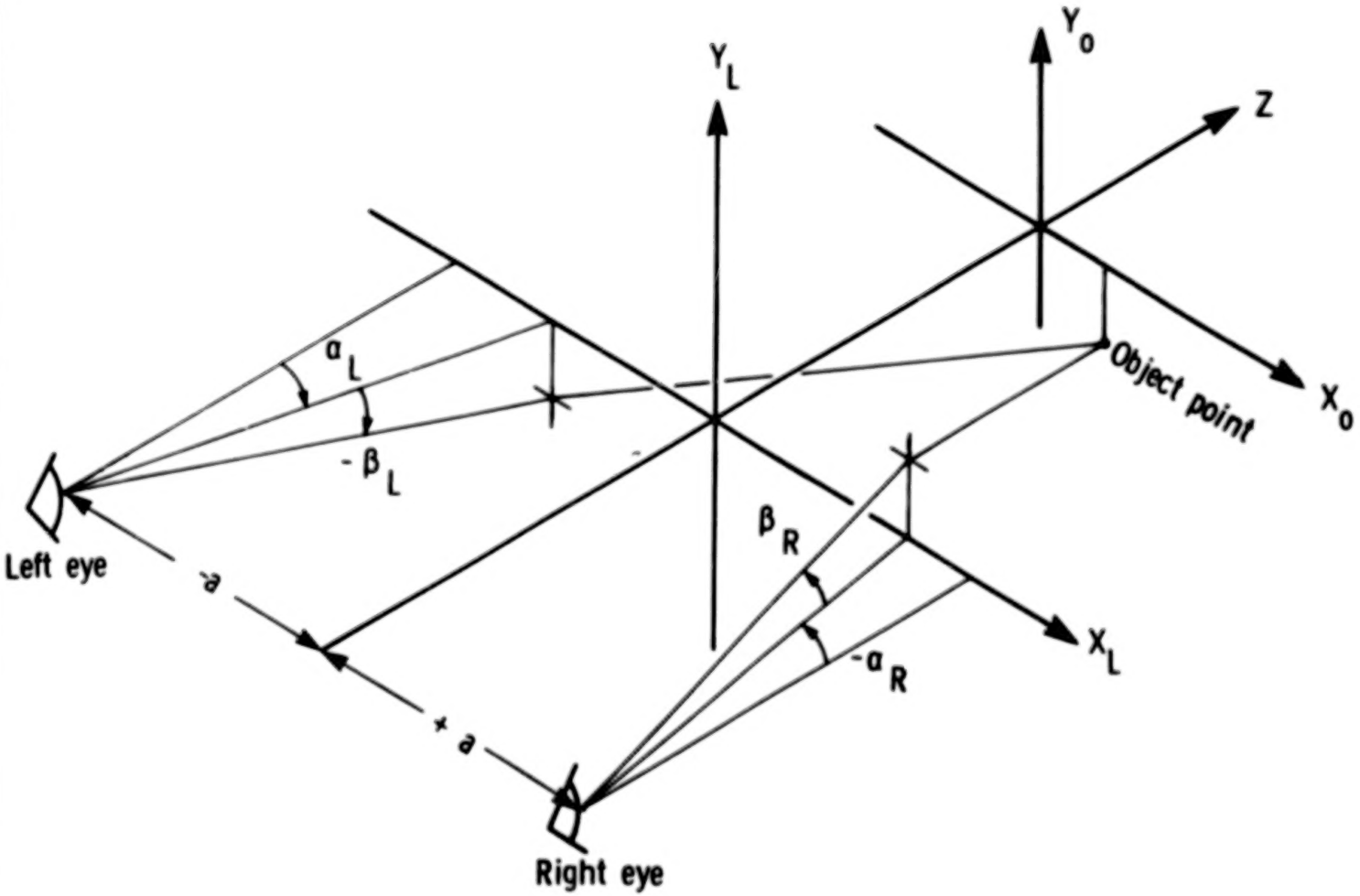

Figure 12.- Geometry for measurement of binocular disparity.

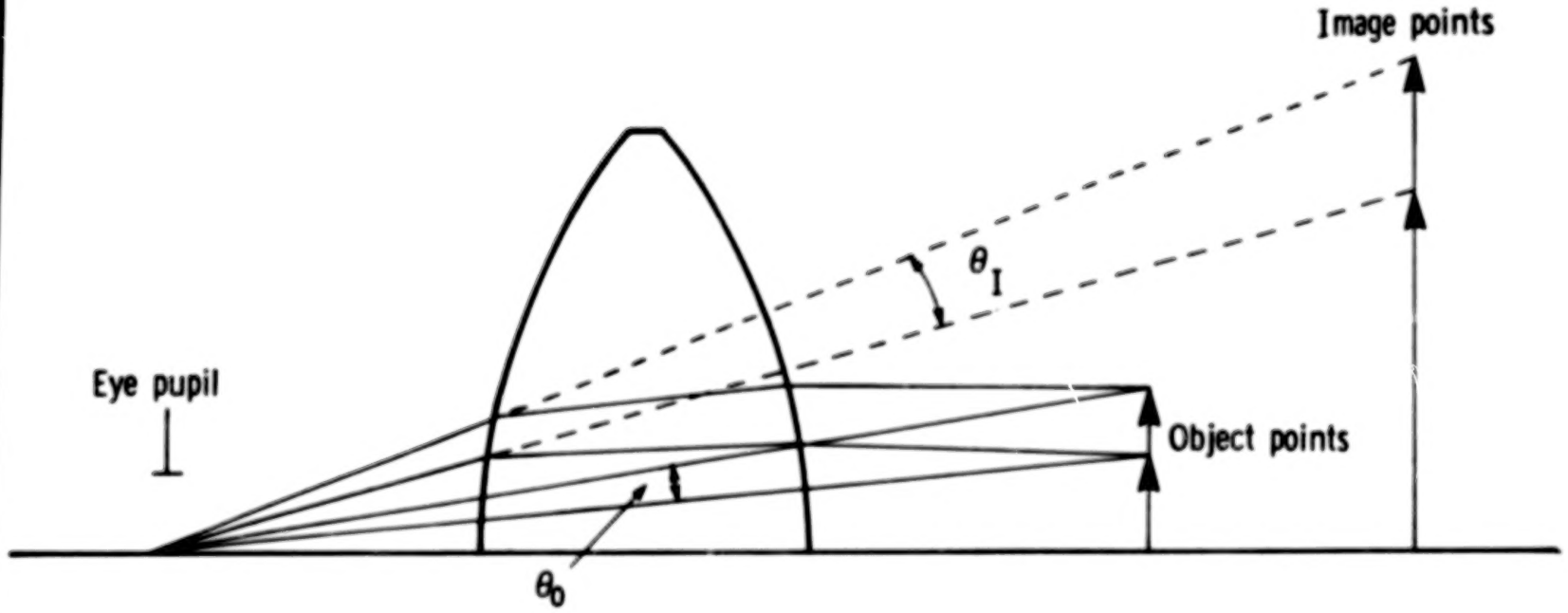

Figure 13.- Geometrical definition of angular magnification.

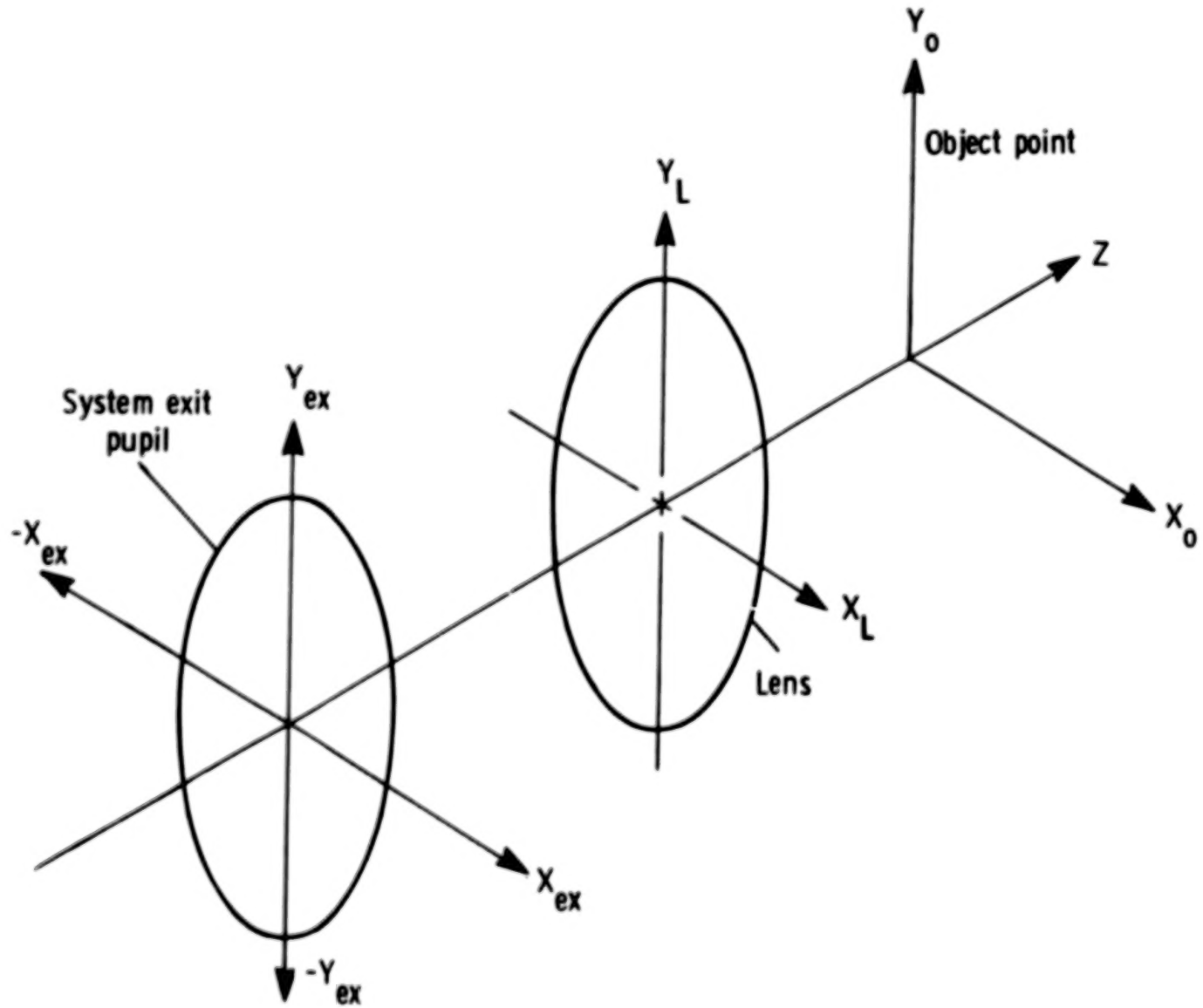

Figure 14.- Ray trace geometry.

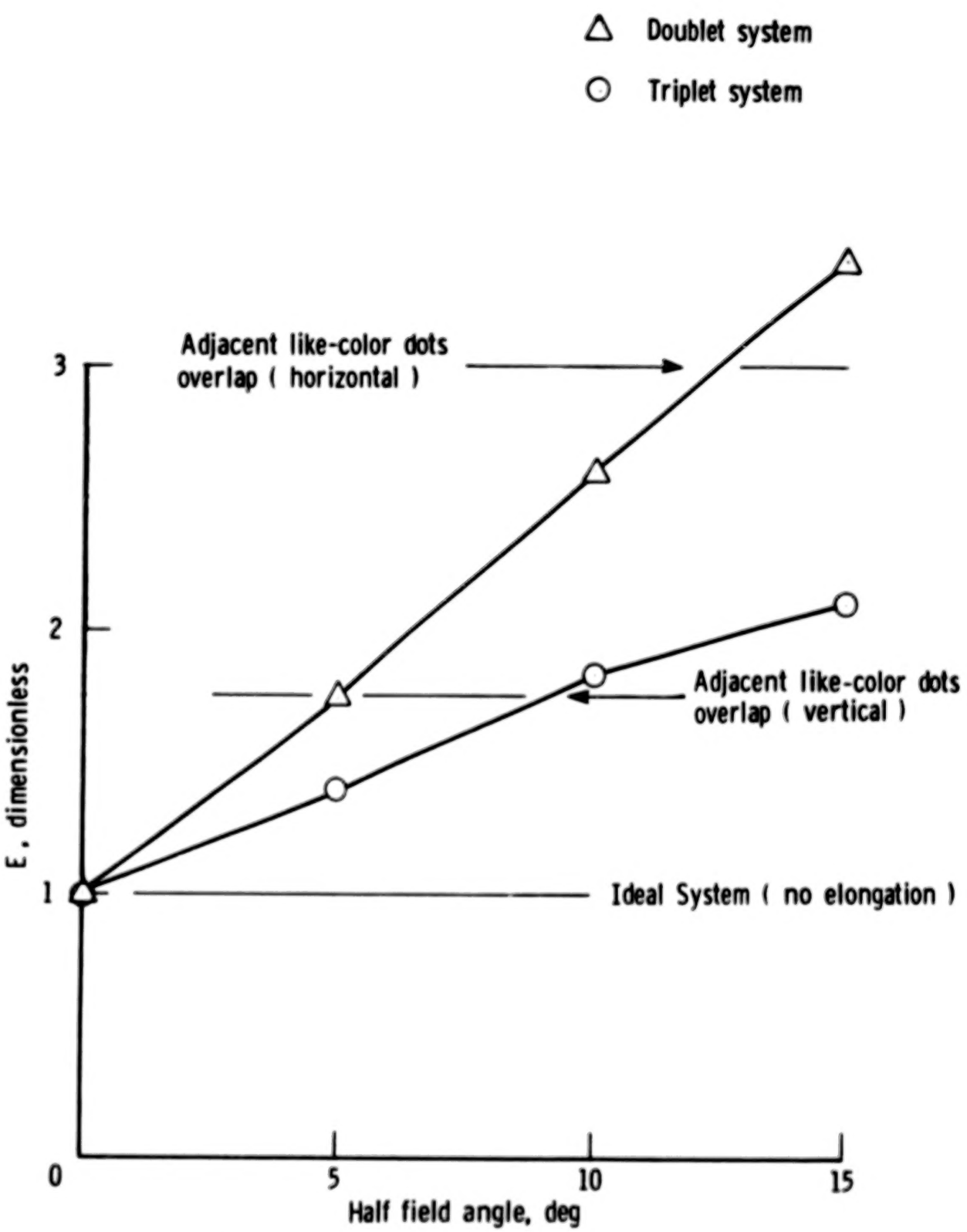

Figure 15.- Dot elongation as a function of half field angle.

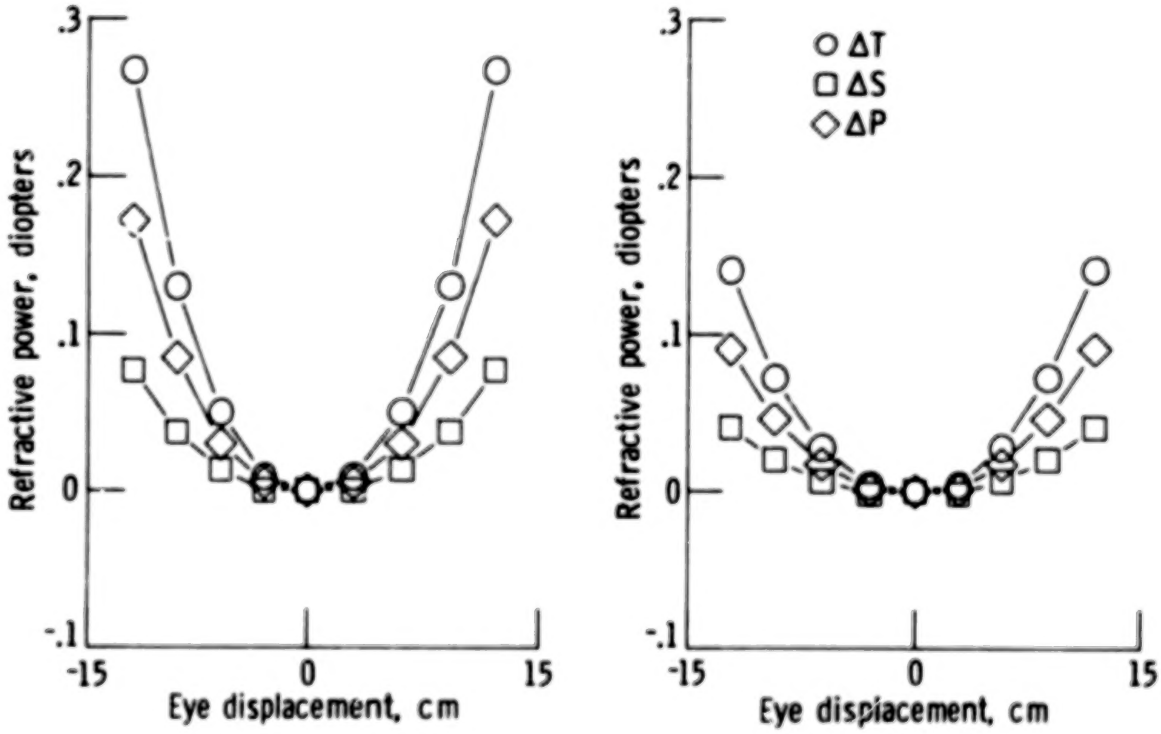

(a) Triplet; half field angle, 0°.

(b) Doublet; half field angle, 0°.

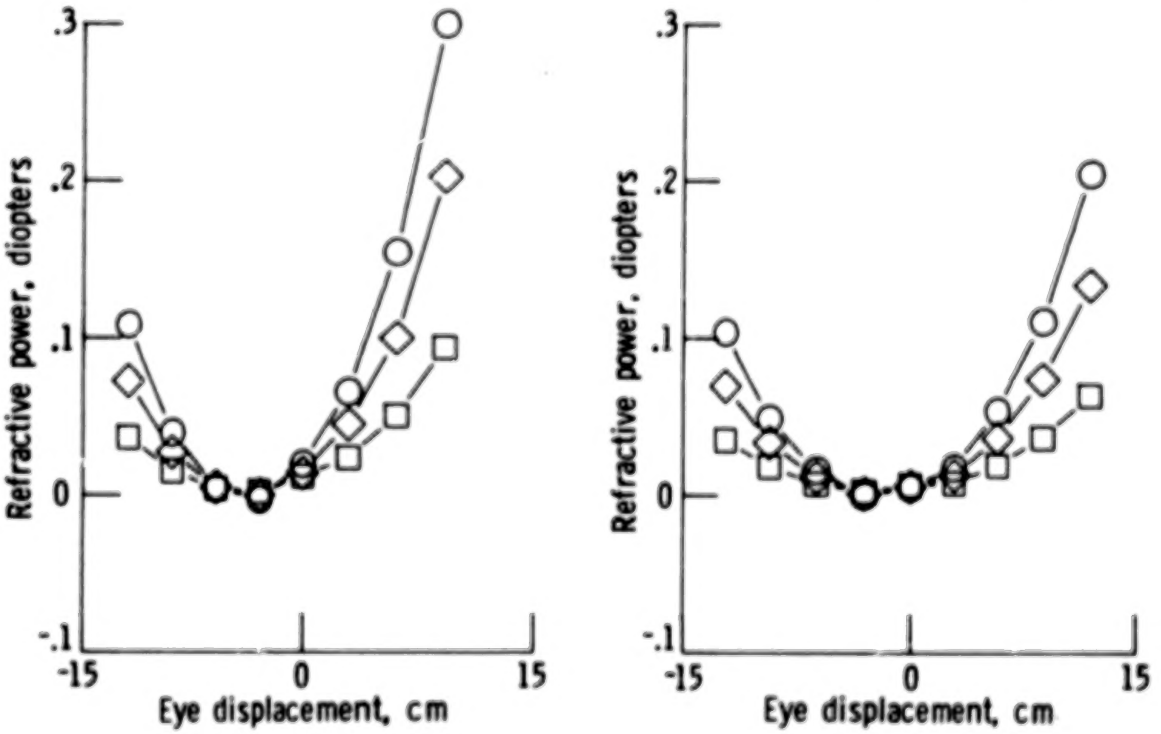

(c) Triplet; half field angle, 5°.

(d) Doublet; half field angle, 5°.

Figure 16.- Plots of ΔT, ΔS, and ΔP.

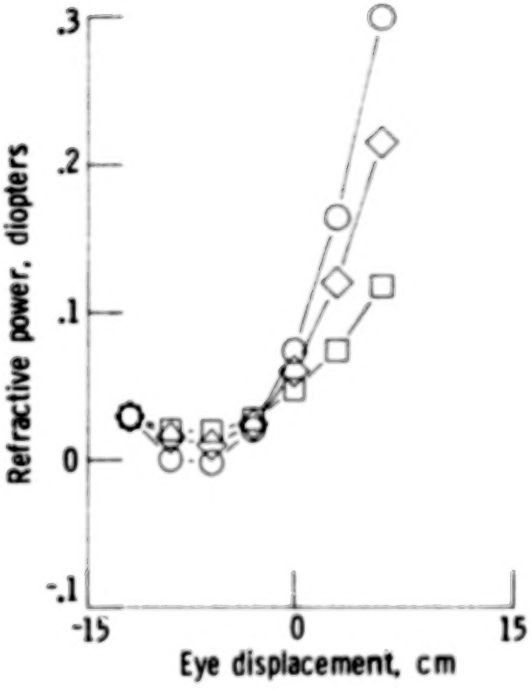

(a) Triplet; half field angle, 10°.

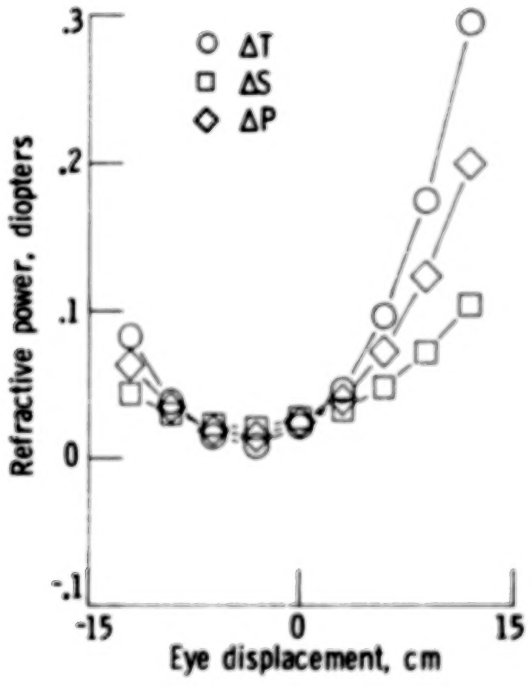

(b) Doublet; half field angle, 10°.

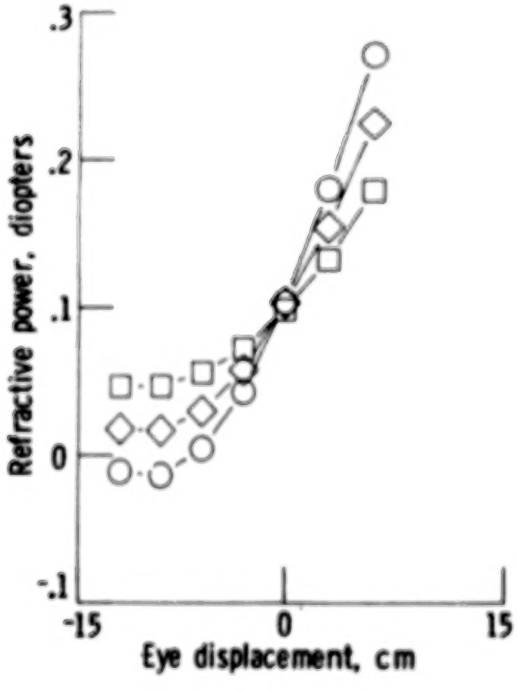

(c) Triplet; half field angle, 15°.

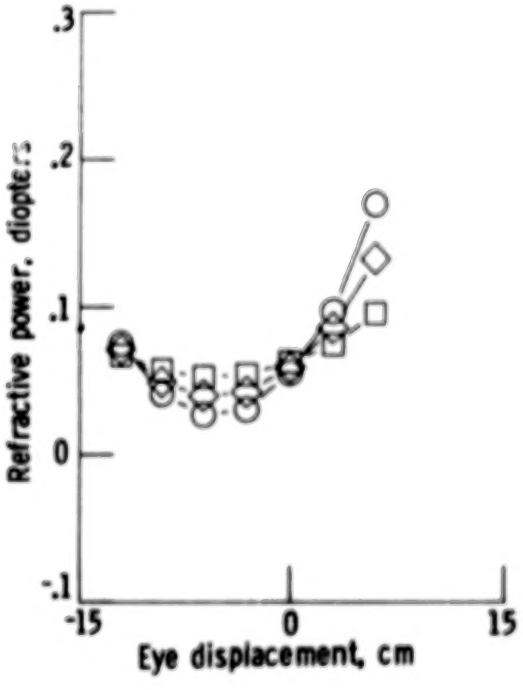

(d) Doublet; half field angle, 15°.

Figure 17.- Plots of ΔT, ΔS, and ΔP.

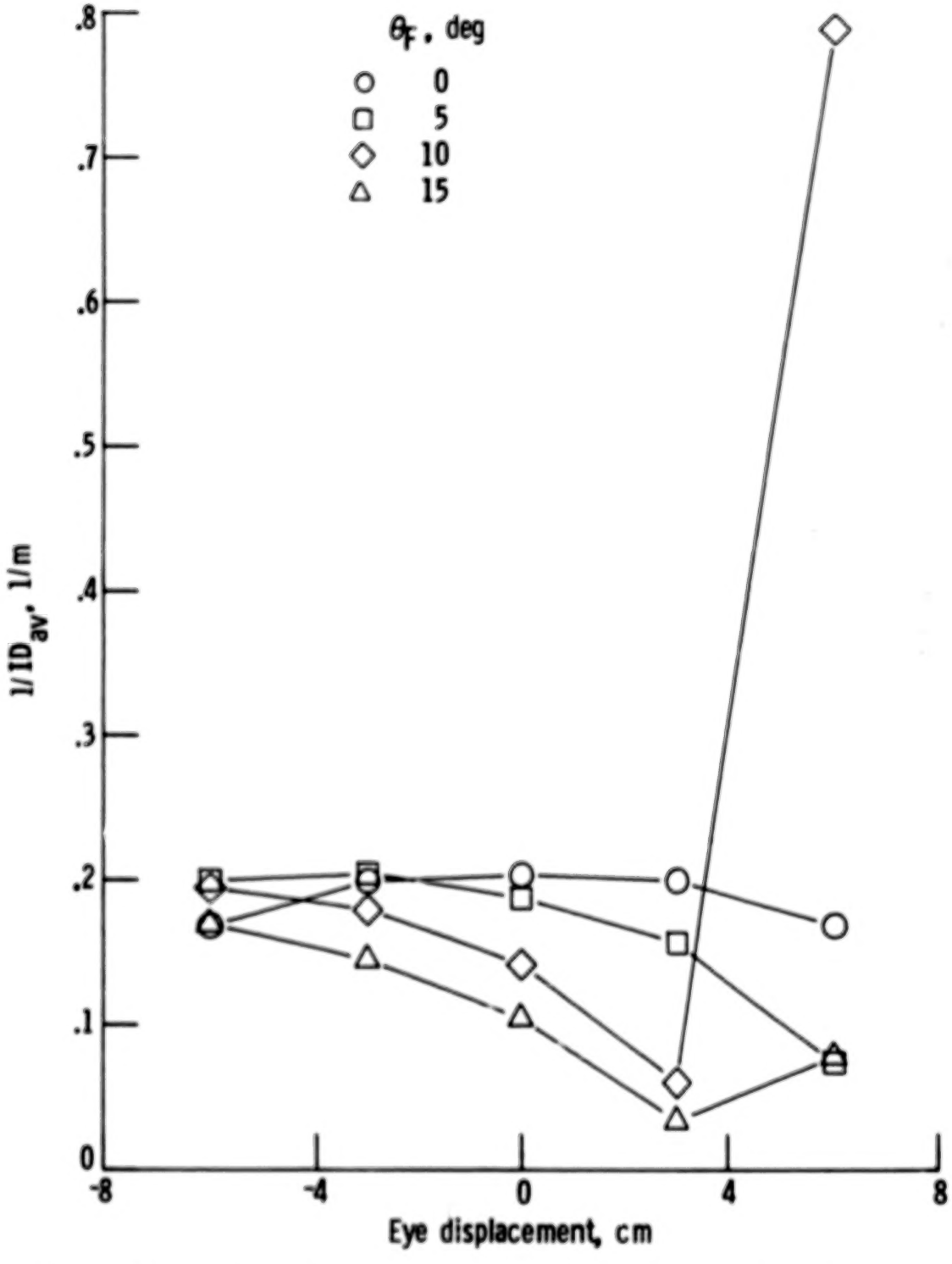

Figure 18.- Reciprocal of average image distance. Triplet; case A.

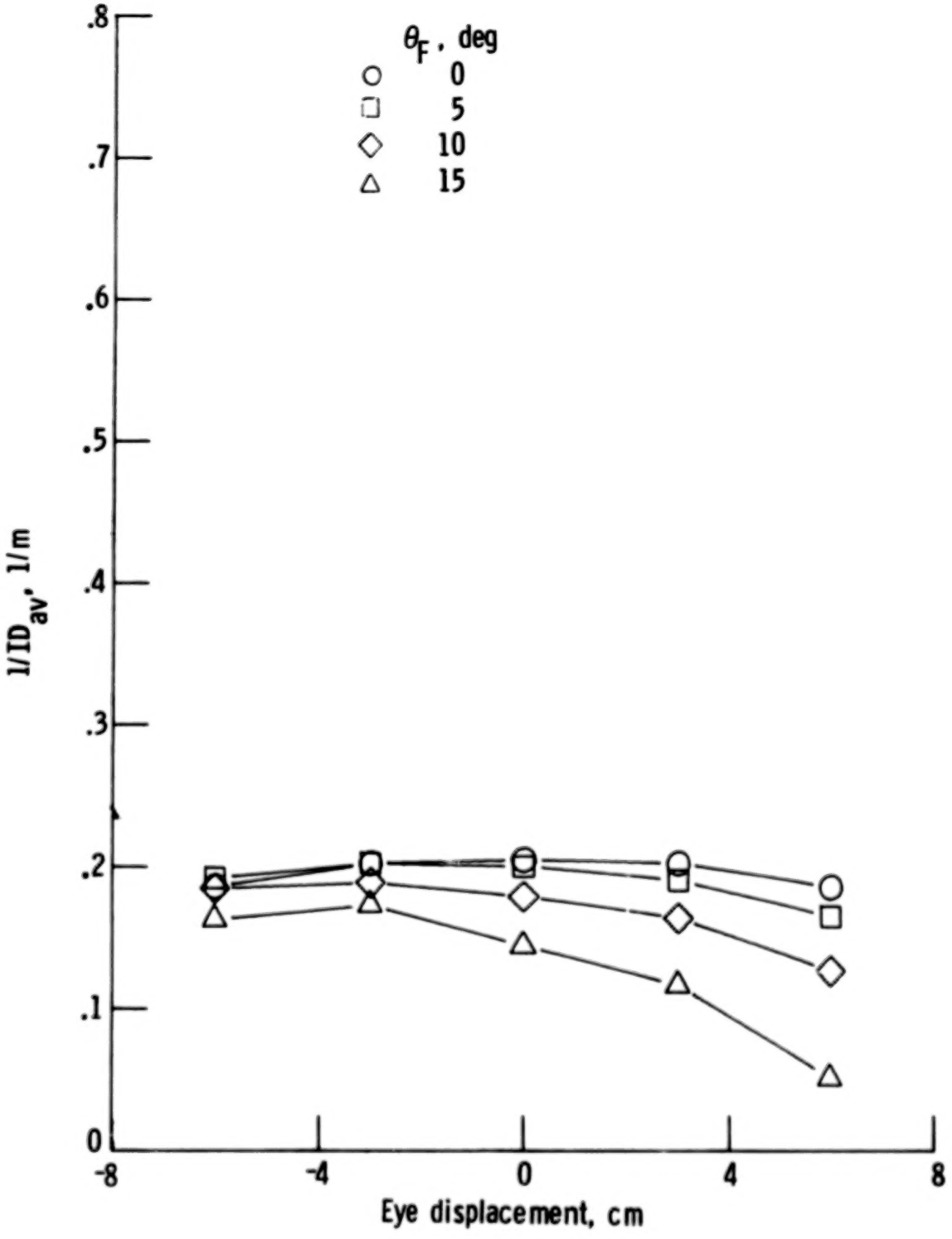

Figure 19.- Reciprocal of average image distance. Doublet; case A.

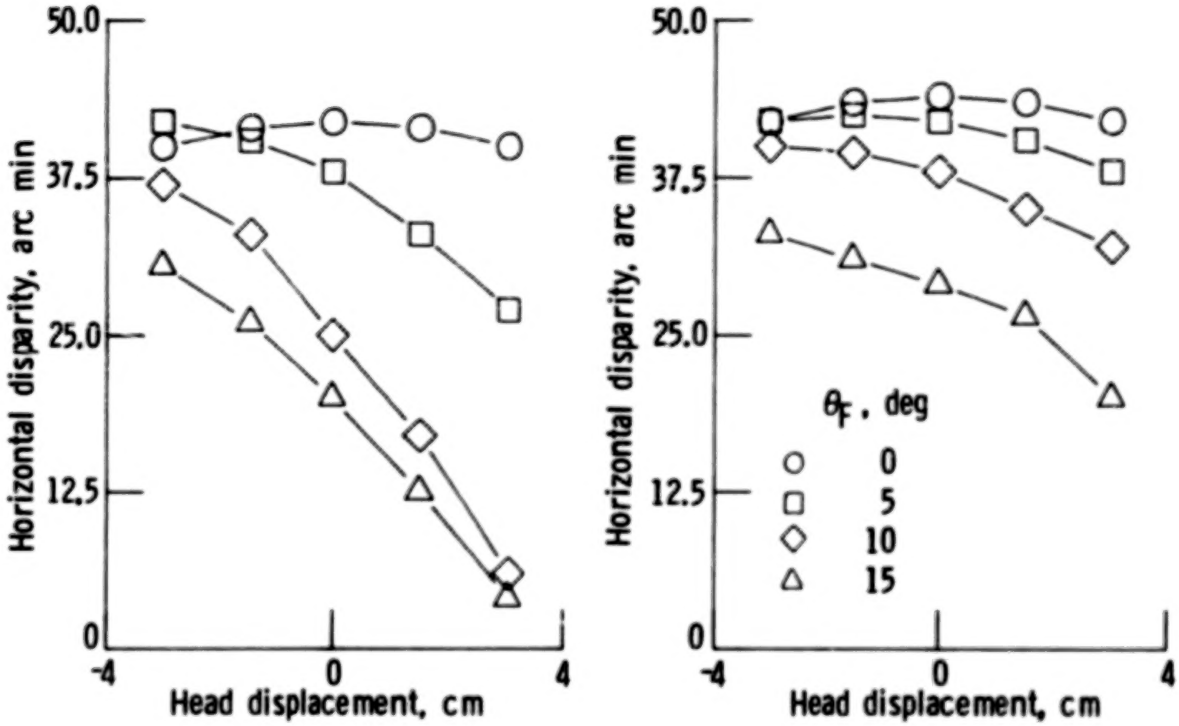

(a) Triplet; case A.

(b) Doublet; case A.

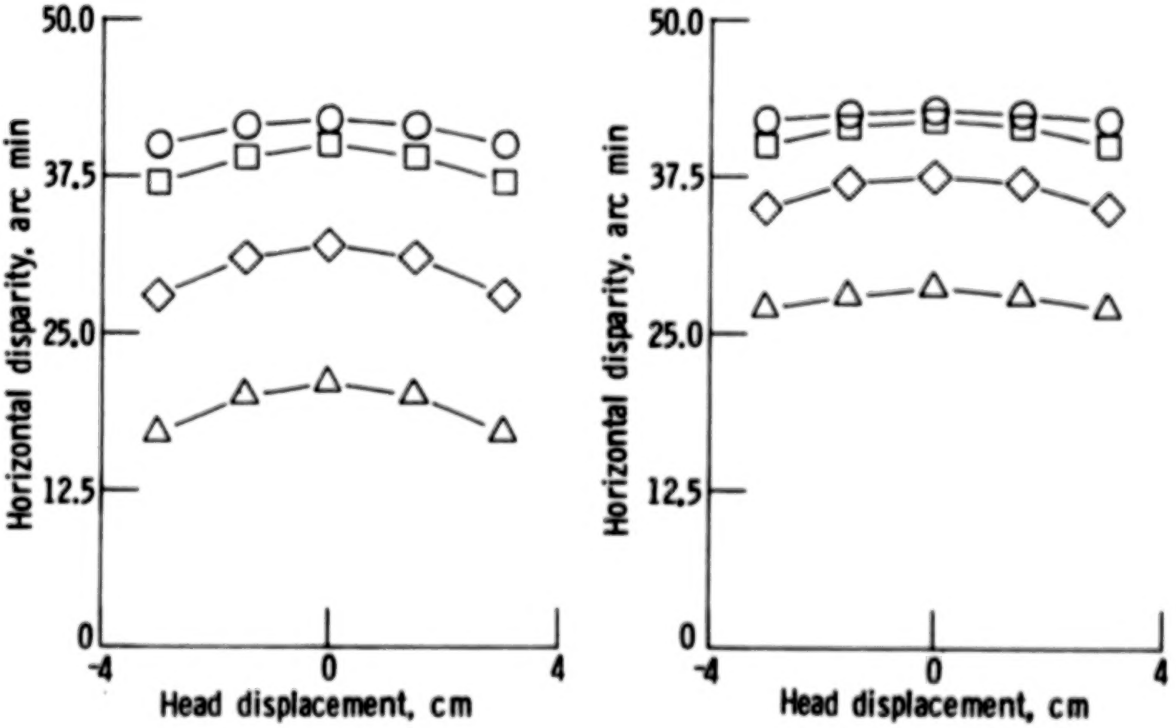

(c) Triplet; case B.

(d) Doublet; case B.

Figure 20.- Horizontal binocular disparity.

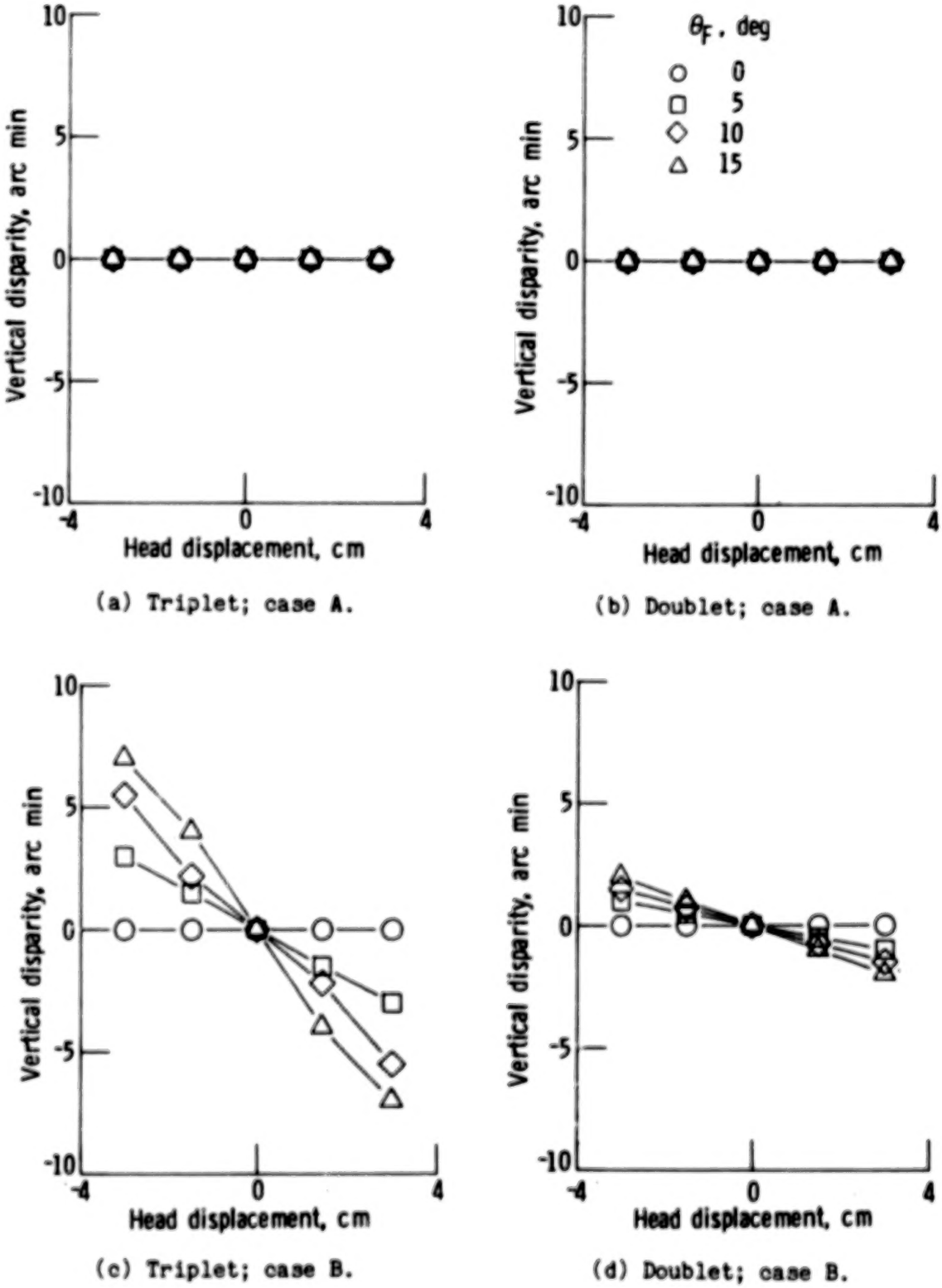

(a) Triplet; case A.

(b) Doublet; case A.

(c) Triplet; case B.

(d) Doublet; case B.

Figure 21.- Vertical binocular disparity.

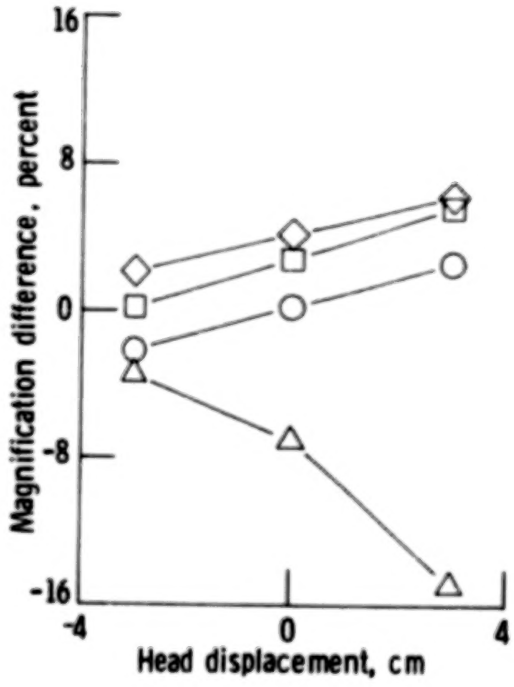

(a) Triplet; case A.

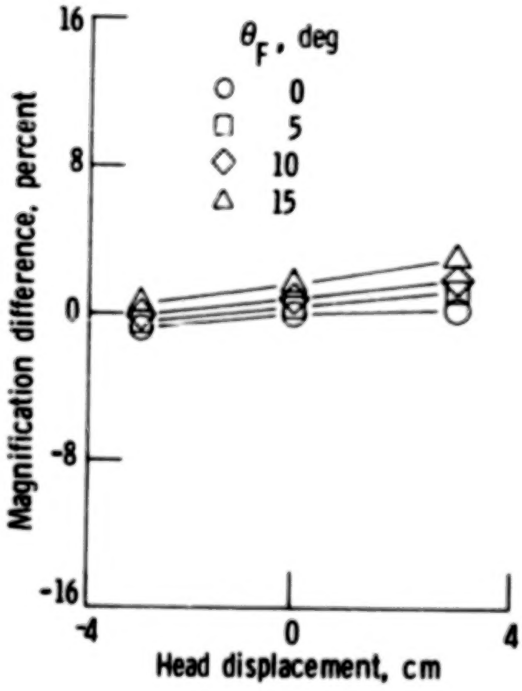

(b) Doublet; case A.

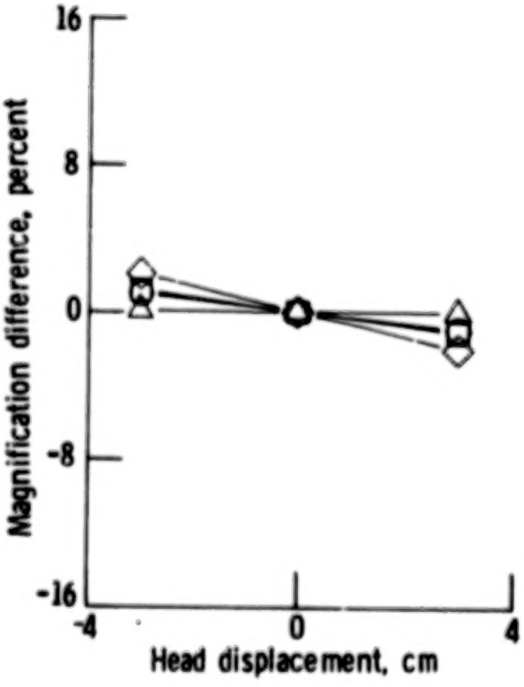

(c) Triplet; case B.

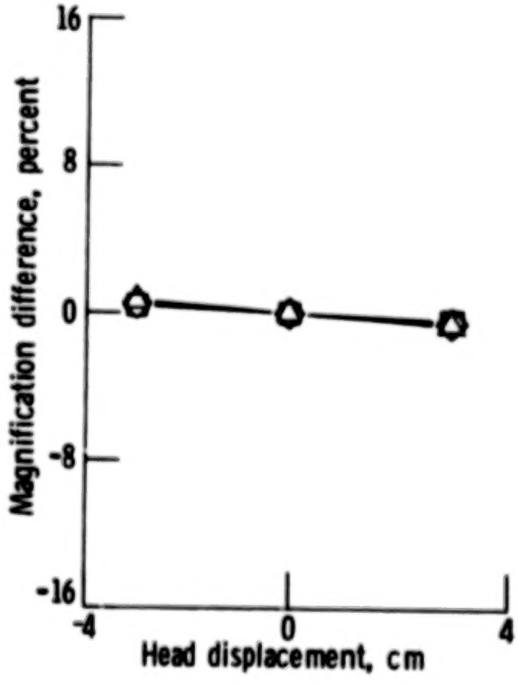

(d) Doublet; case B.

Figure 22.- Binocular magnification differences.

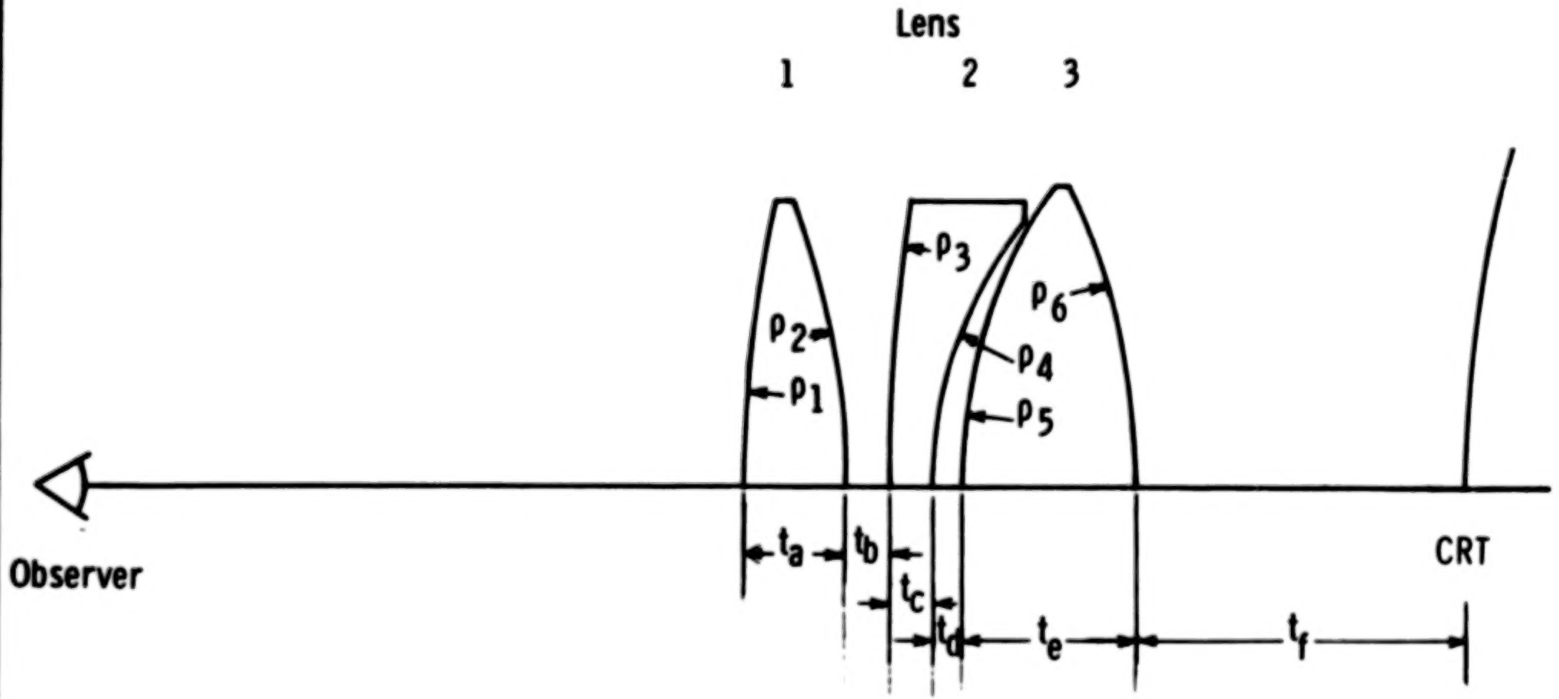

Figure 23.- Basic triplet layout.

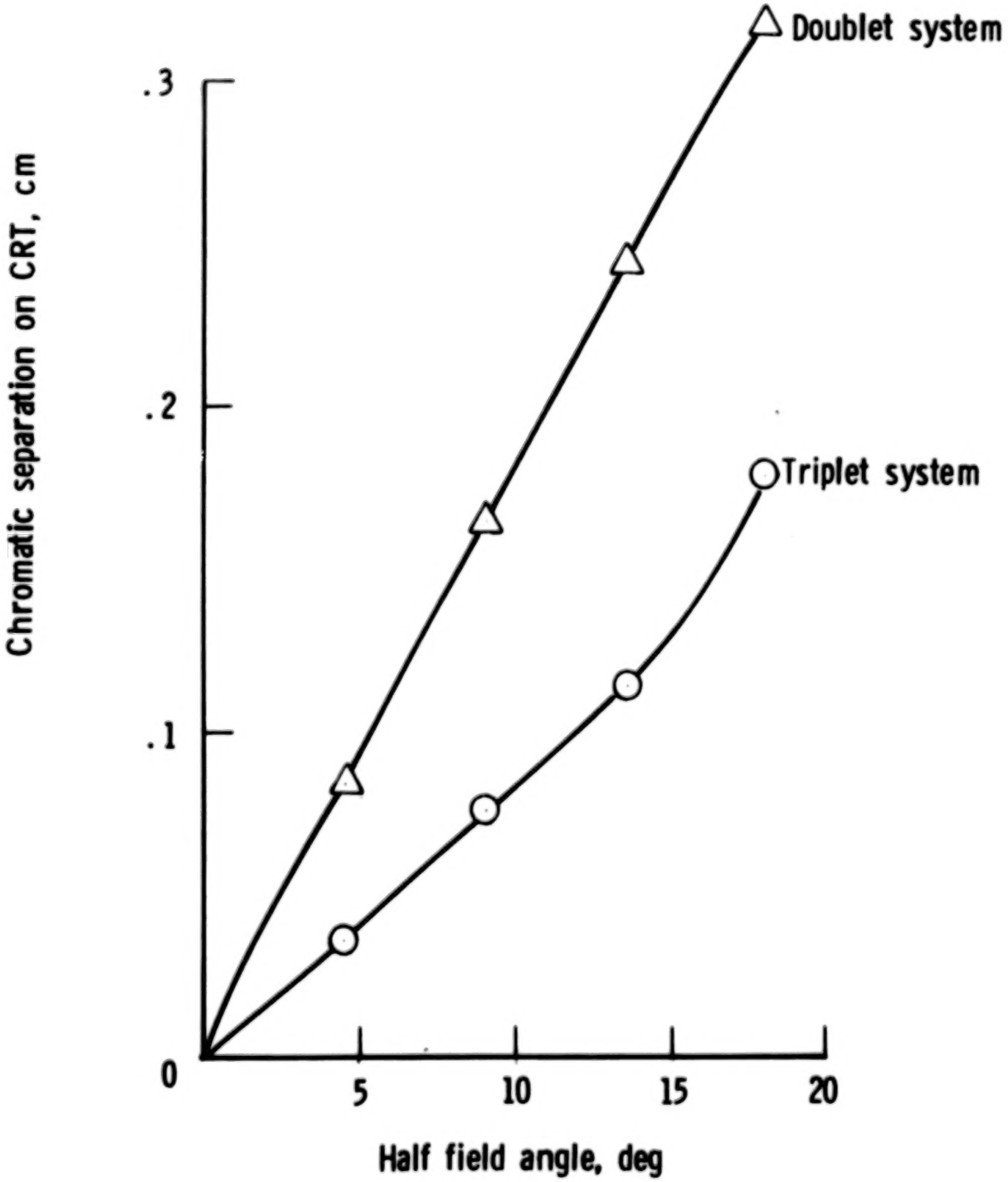

Figue 24.- Comparison of chromatic separation on CRT between triplet system and doublet system.

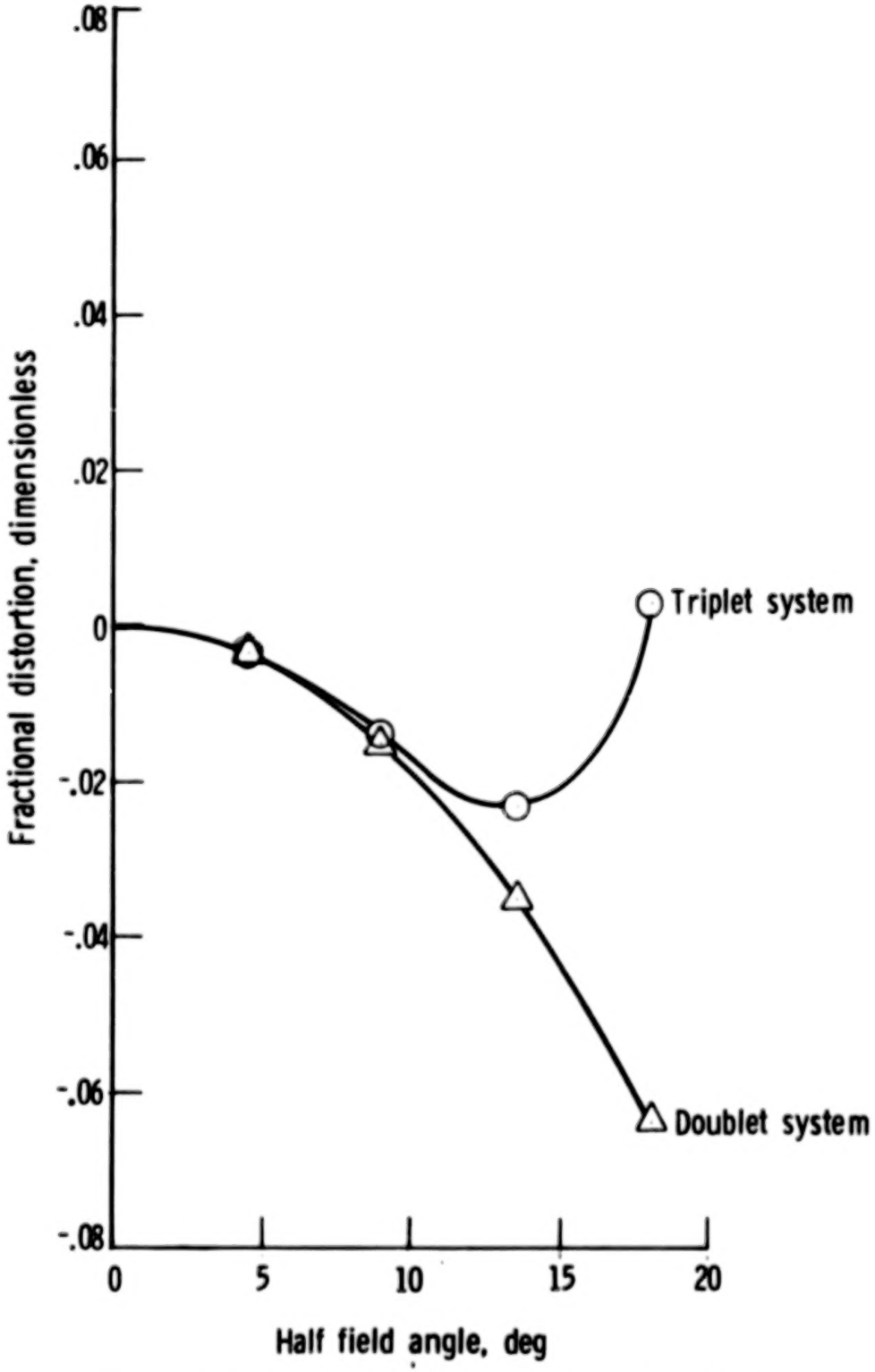

Figure 25.- Comparison of fractional distortion between triplet system and doublet system.

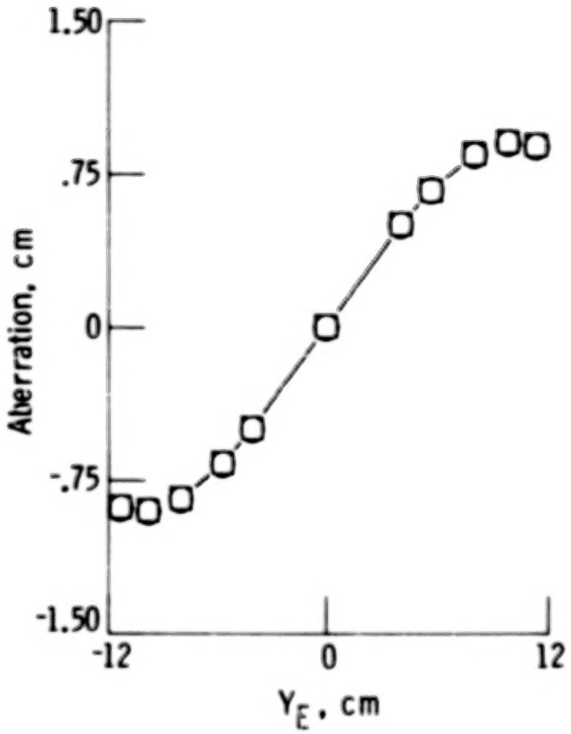

(a) Triplet; half field angle, 0°.

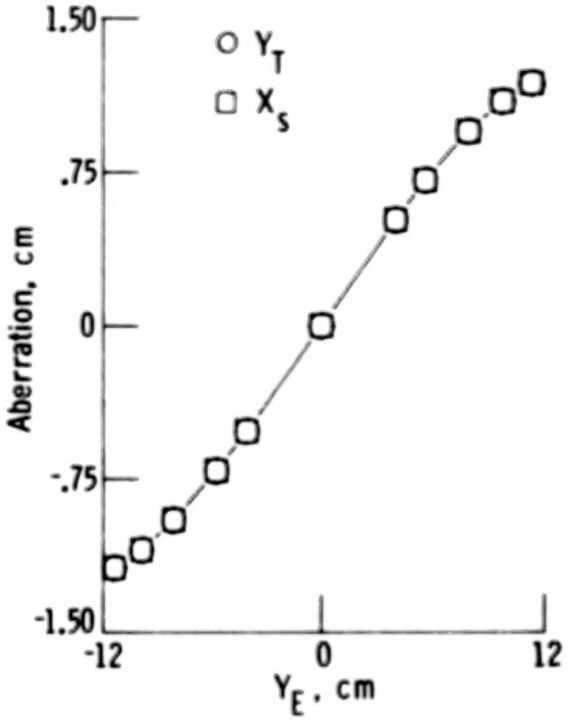

(b) Doublet; half field angle, 0°.

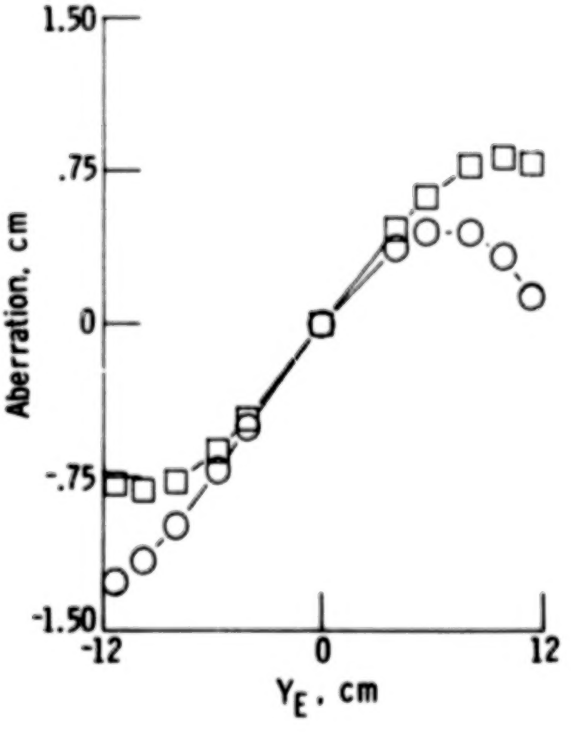

(c) Triplet; half field angle, 5°.

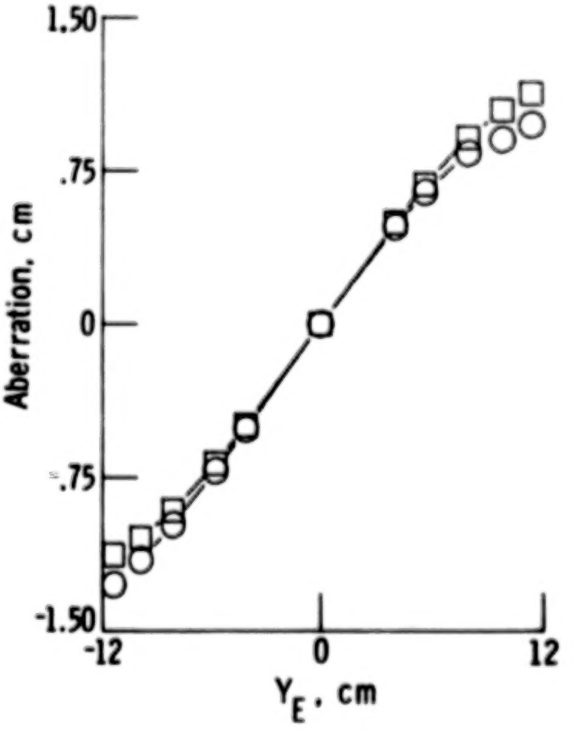

(d) Doublet; half field angle, 5°.

Figure 26.- Monochromatic aberrations for 0° and 5° half field angles.

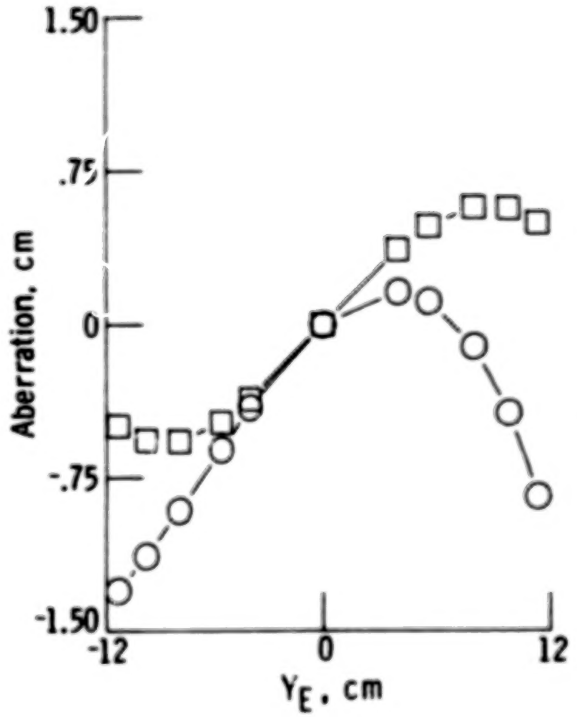

(a) Triplet; half field angle, 10°.

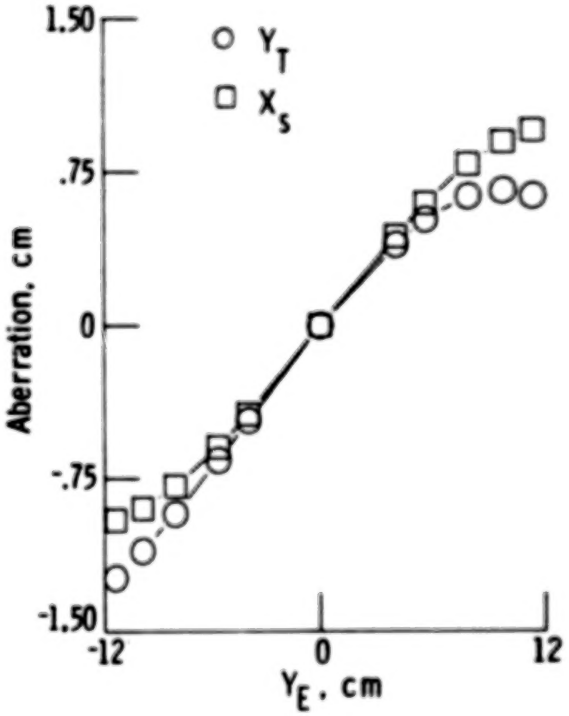

(b) Doublet; half field angle, 10°.

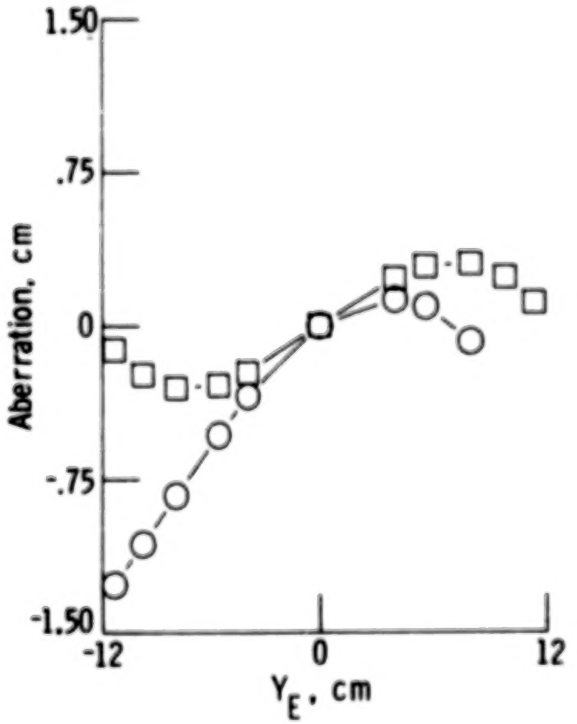

(c) Triplet; half field angle, 15°.

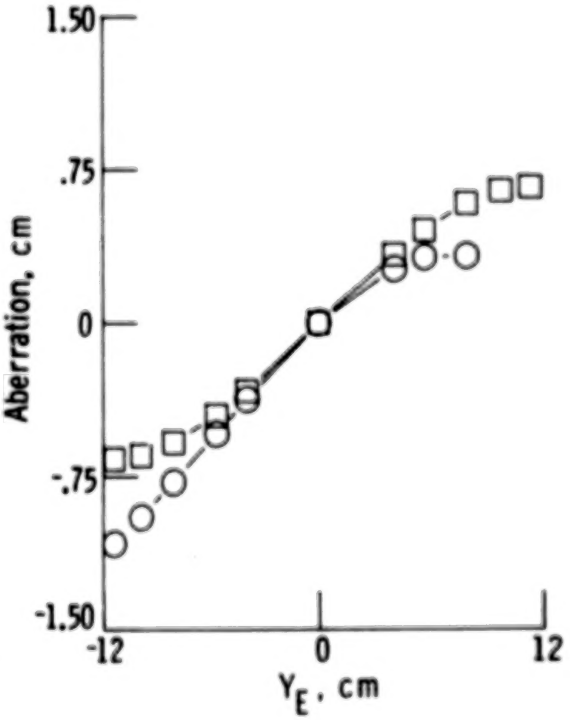

(d) Doublet; half field angle, 15°.

Figure 27.- Monochromatic aberrations for 10° and 15° half field angles.

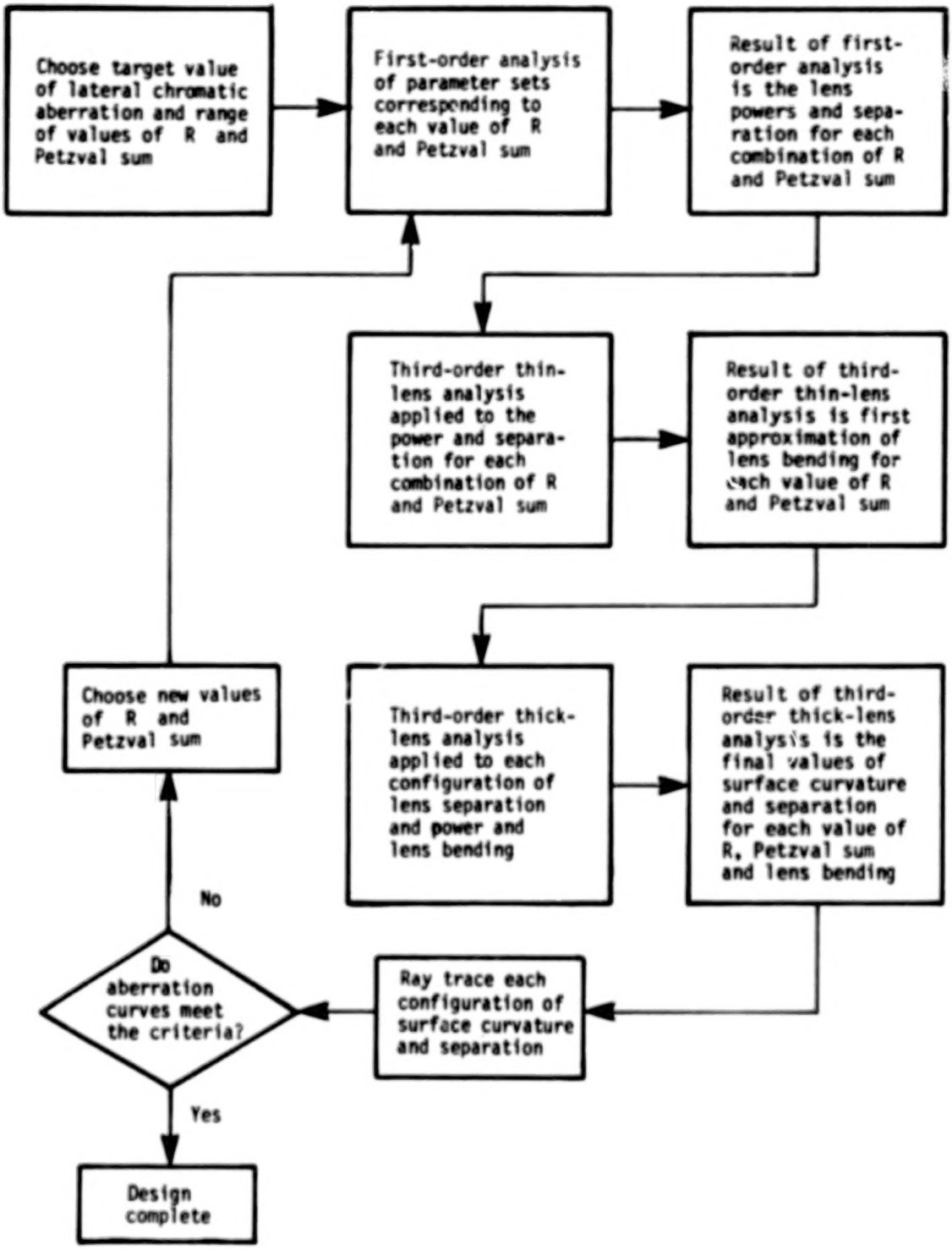
Choose target value of lateral chromatic aberration and range of values of R and Petzval sum
First-order analysis of parameter sets corresponding to each value of R and Petzval sum
Result of first-order analysis is the lens powers and separation for each combination of R and Petzval sum
Third-order thin-lens analysis applied to the power and separation for each combination of R and Petzval sum
Result of third-order thin-lens analysis is first approximation of lens bending for each value of R and Petzval sum
Choose new values of R and Petzval sum
Third-order thick-lens analysis applied to each configuration of lens separation and power and lens bending
Result of third-order thick-lens analysis is the final values of surface curvature and separation for each value of R, Petzval sum and lens bending
No
Do aberration curves meet the criteria?
Ray trace each configuration of surface curvature and separation
Yes
Design complete

Figure 28.- Outline of design procedure.

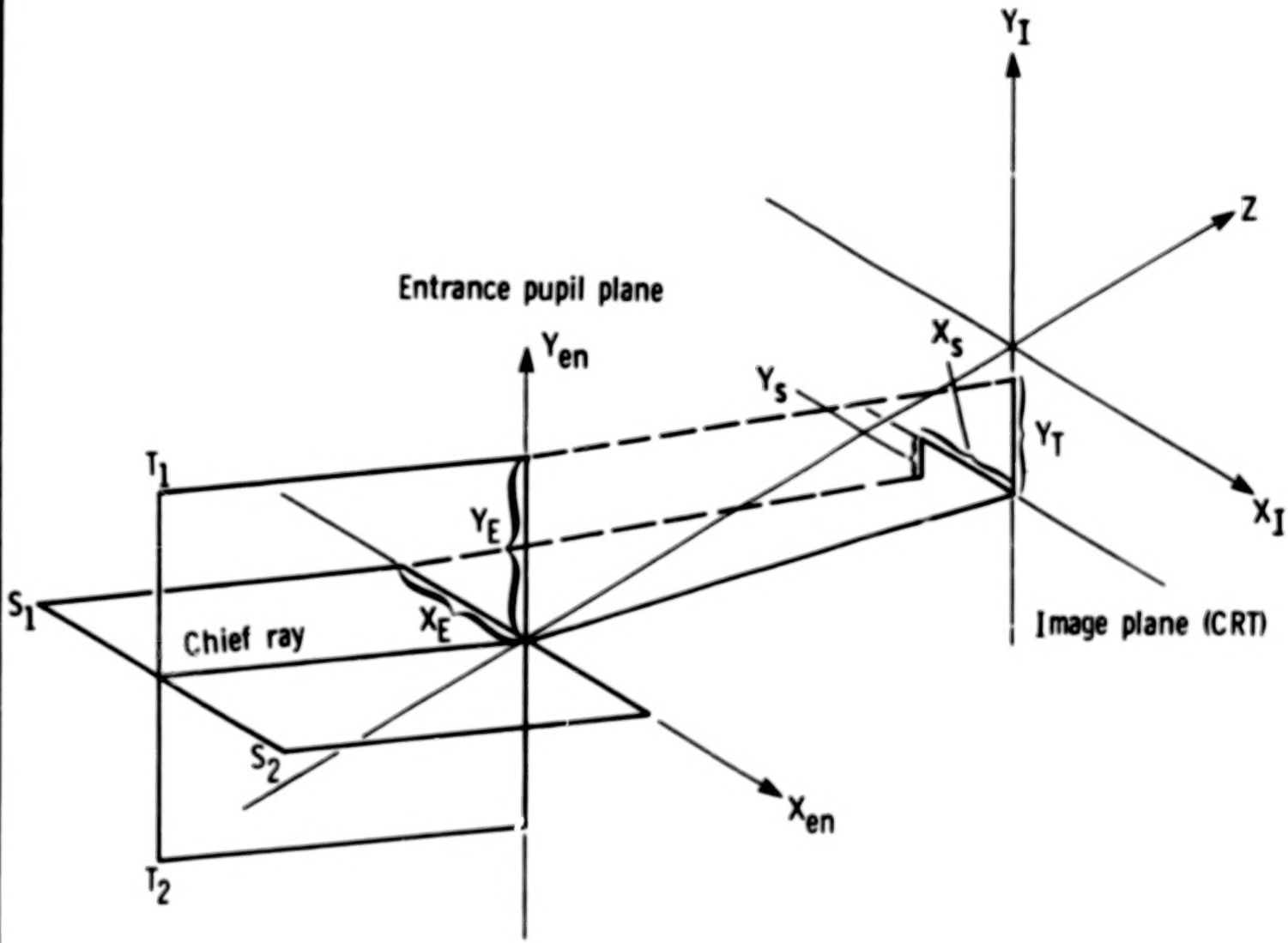

Figure 29.- Definition of aberration curve coordinates.

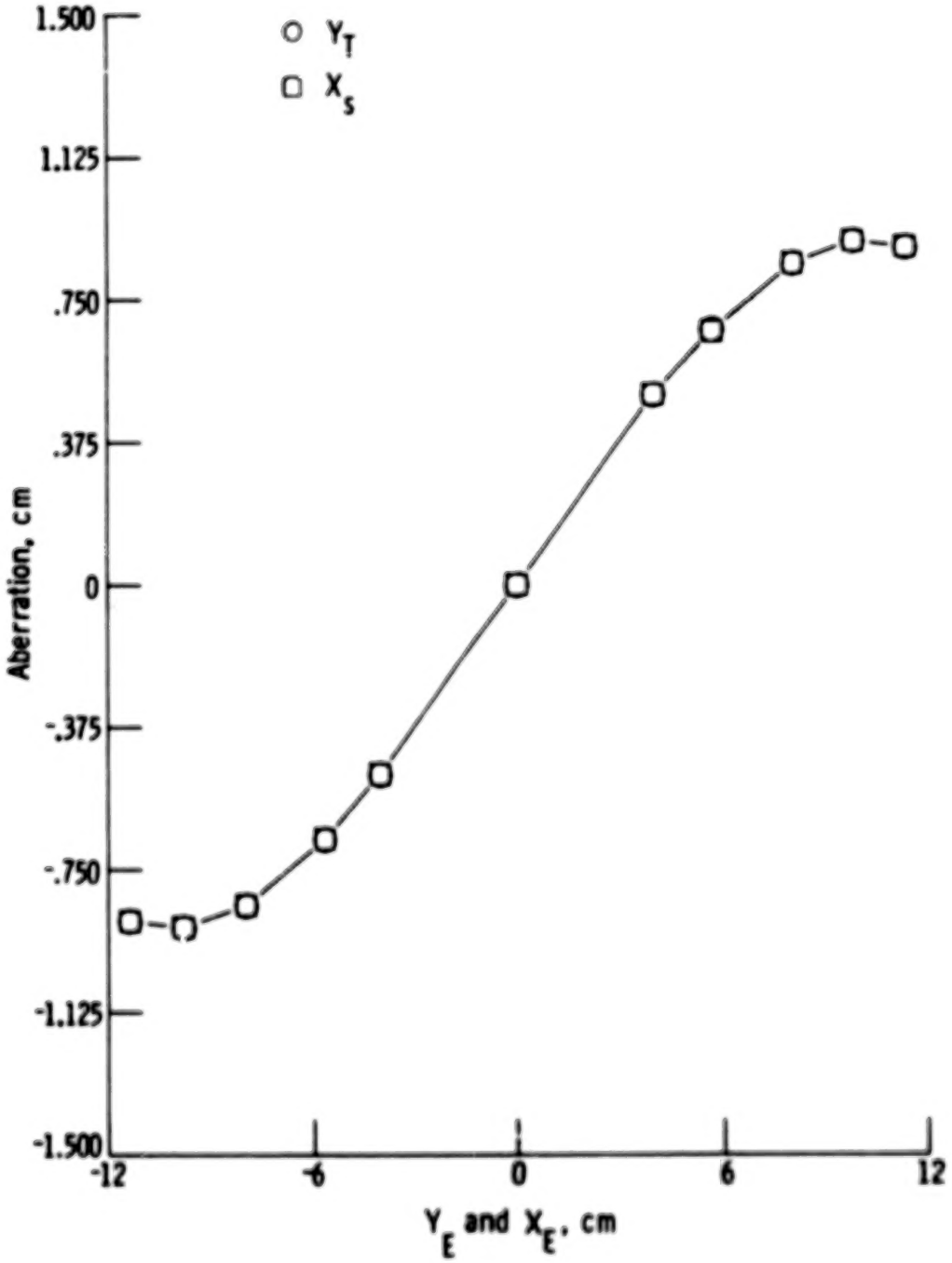

Figure 30.- Variation of Y_T with Y_E and X_S with X_E for zero half field angle.

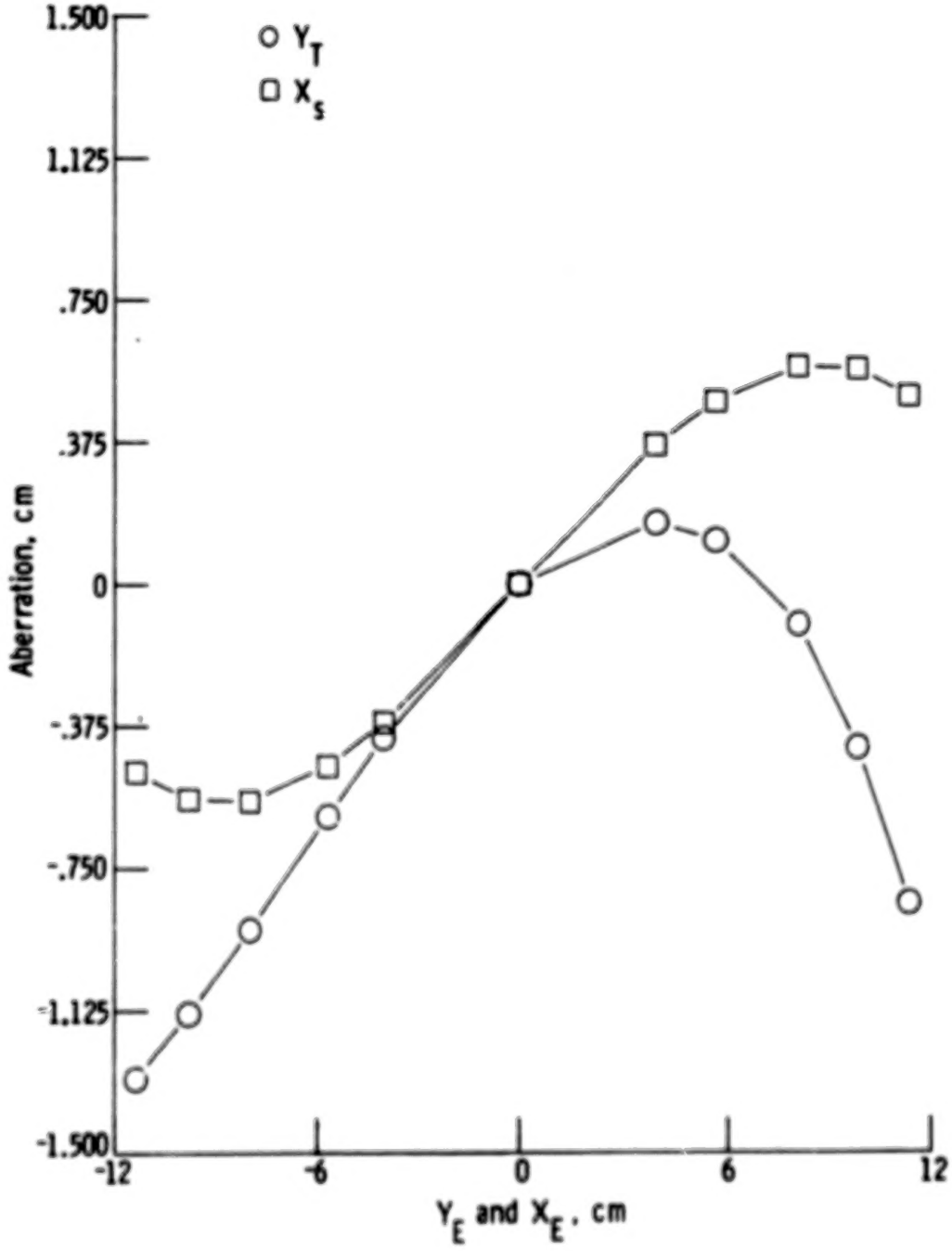

Figure 31.- Variation of Y_T with Y_E and X_s with X_E for 10° half field angle.

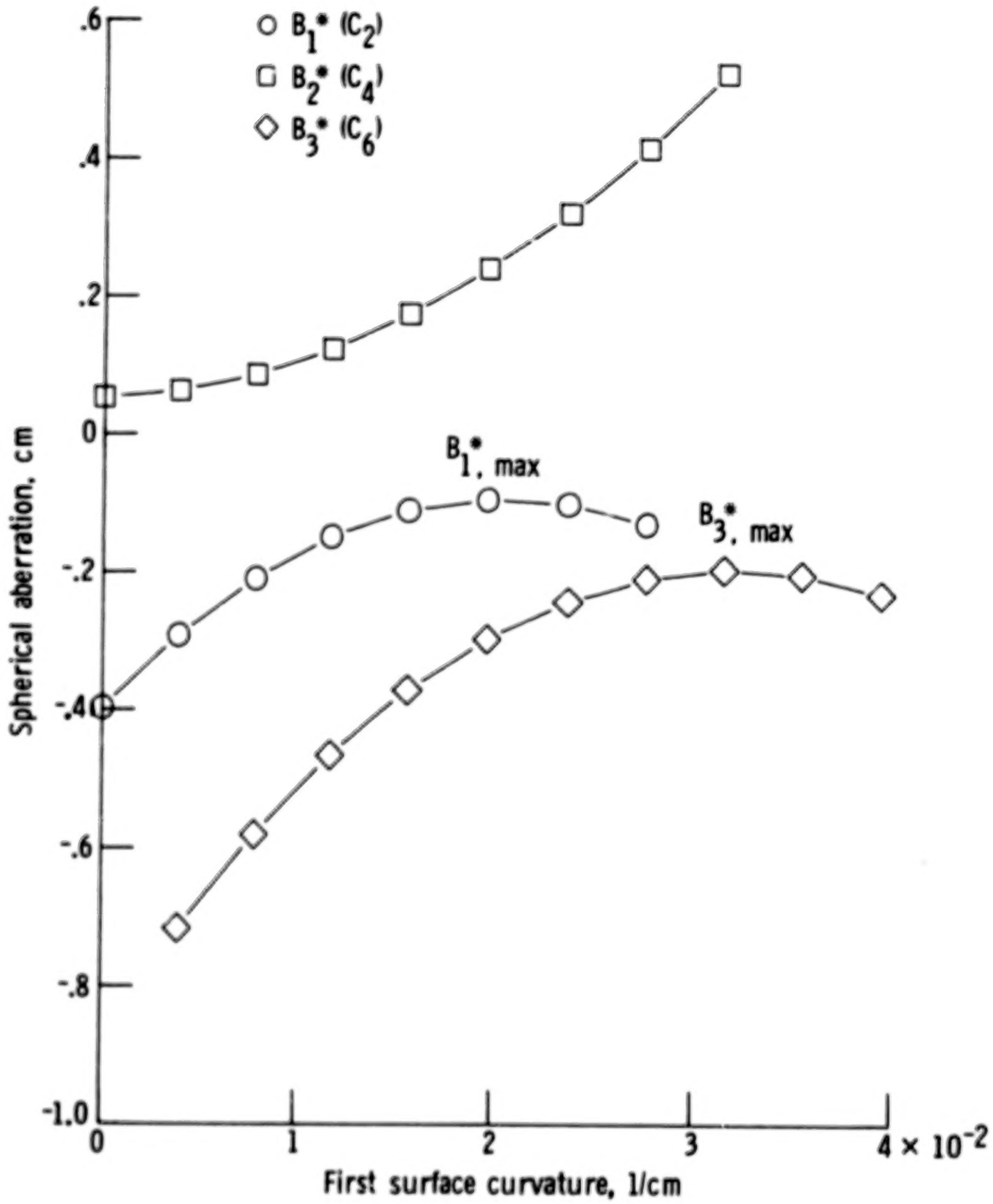

Figure 32.- Variation of spherical aberration with first surface curvature.

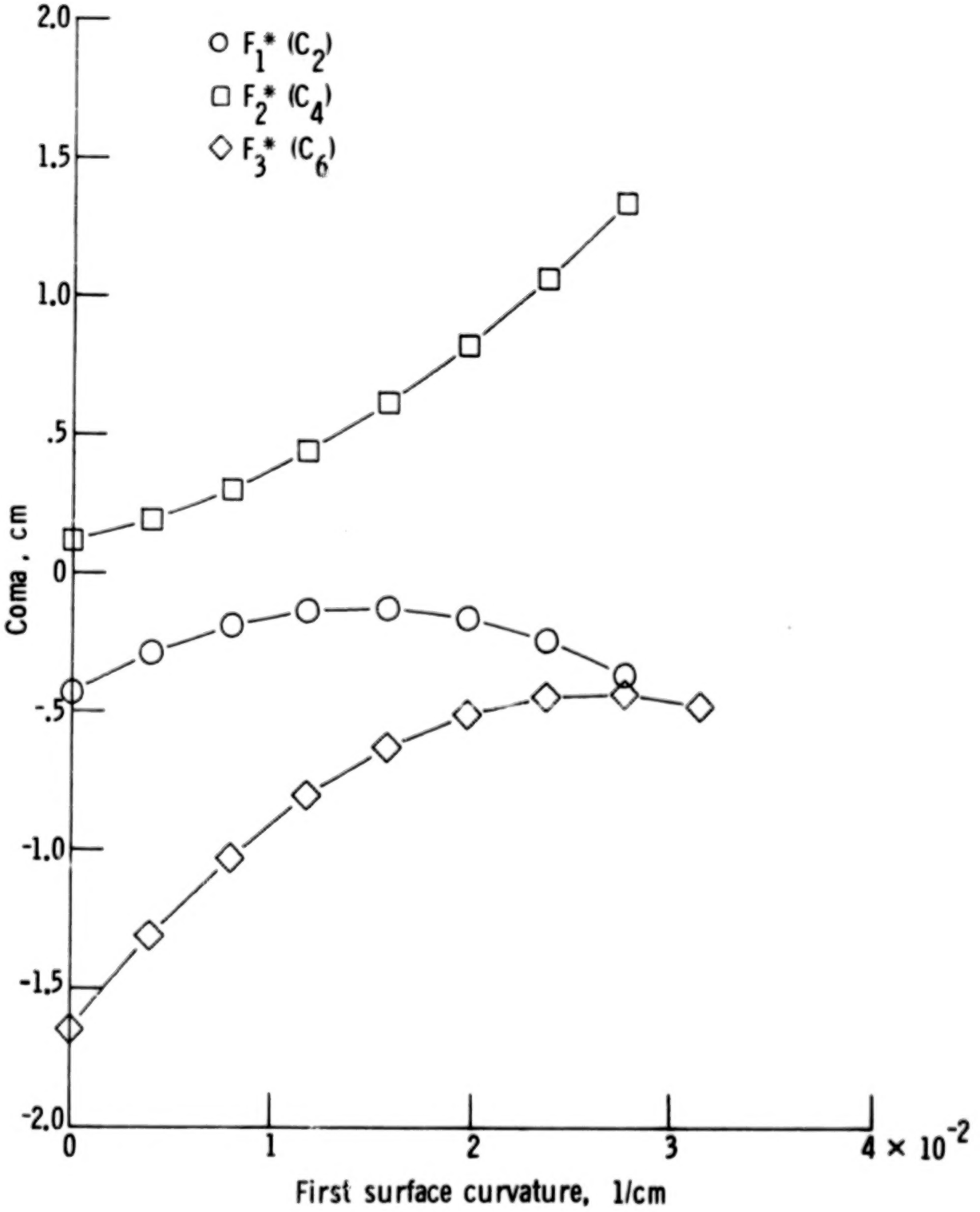

Figure 33.- Variation of coma with first surface curvature.

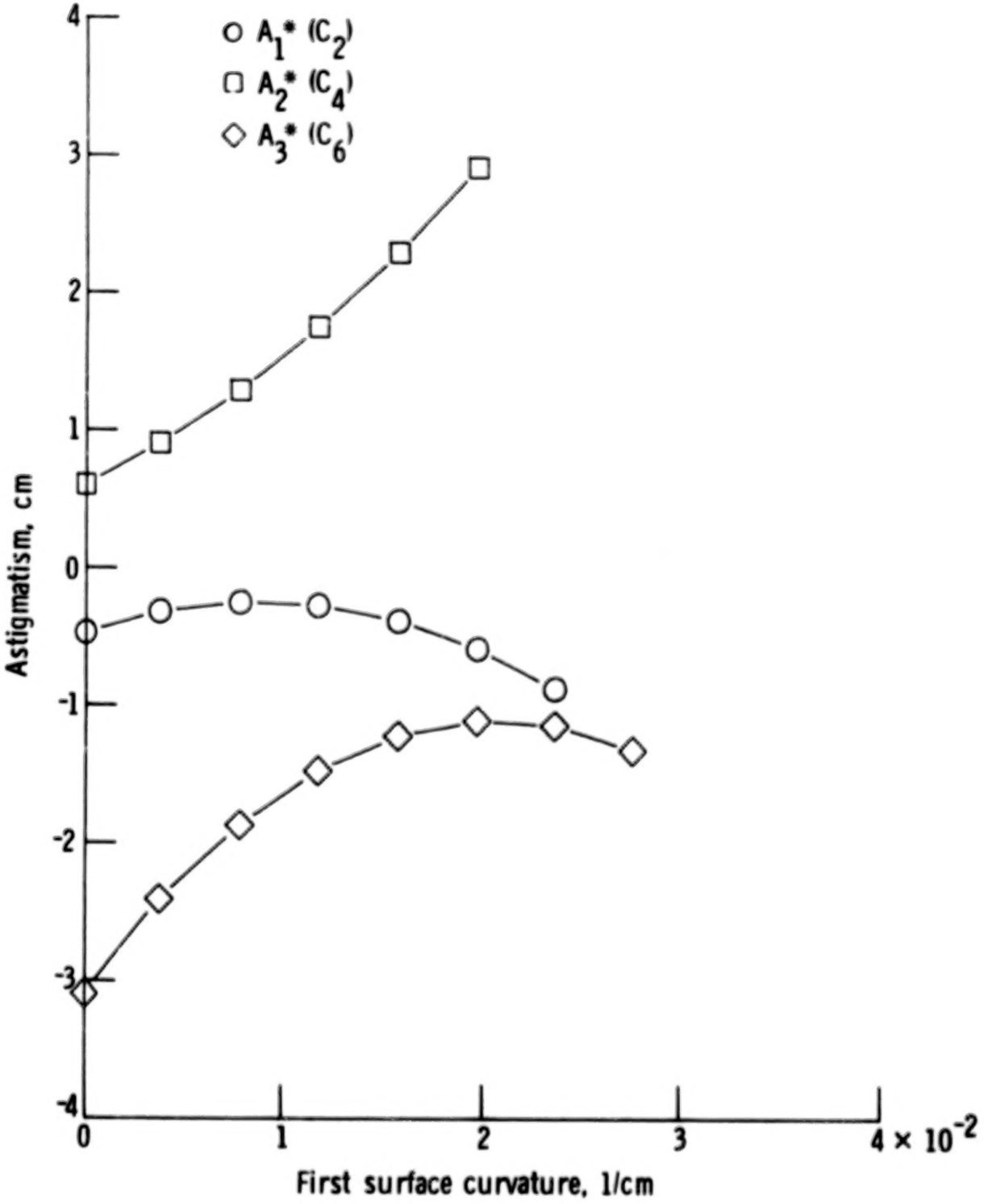

Figure 34.- Variation of astigmatism with first surface curvature.

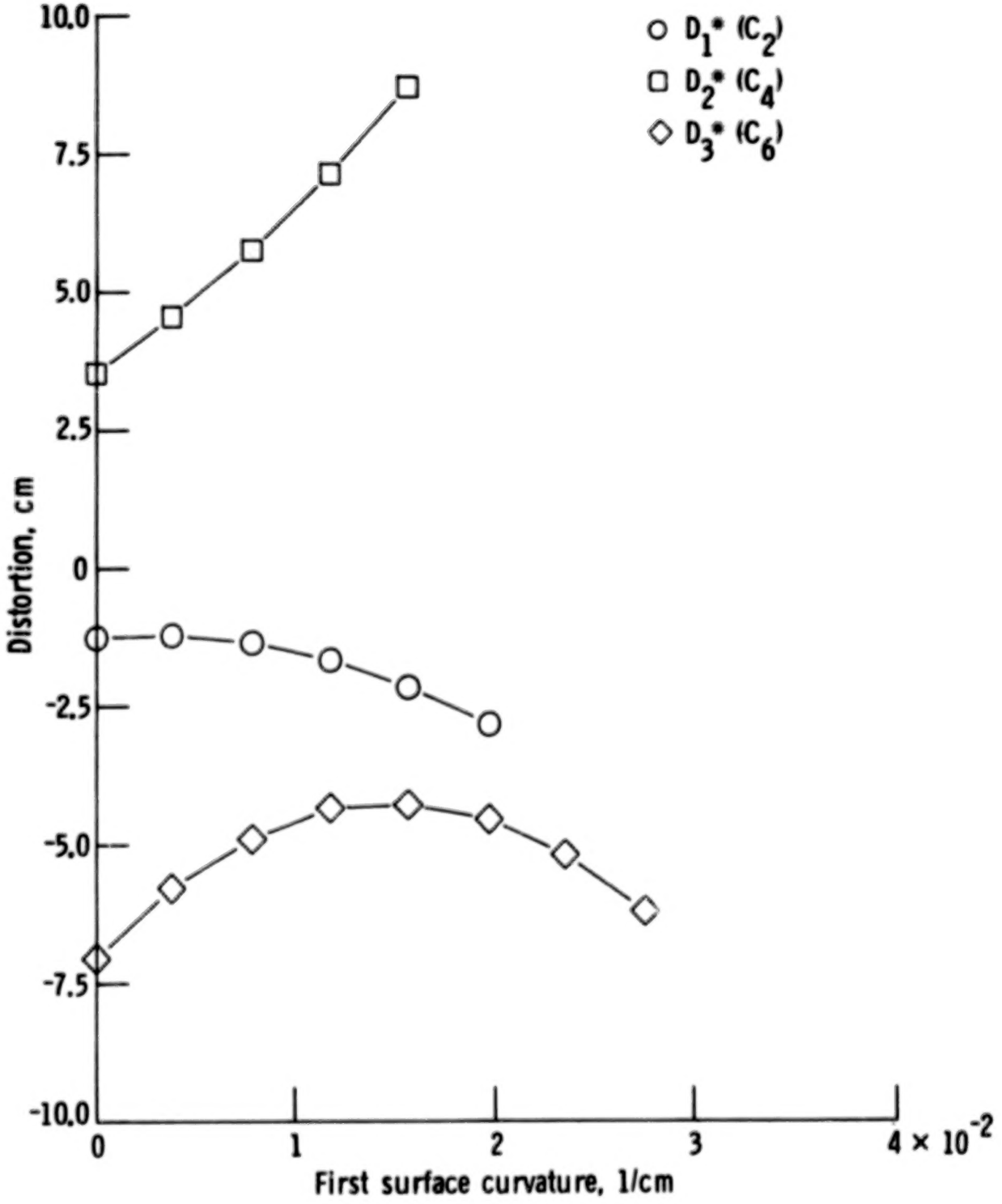

Figure 35.- Variation of distortion with first surface curvature.

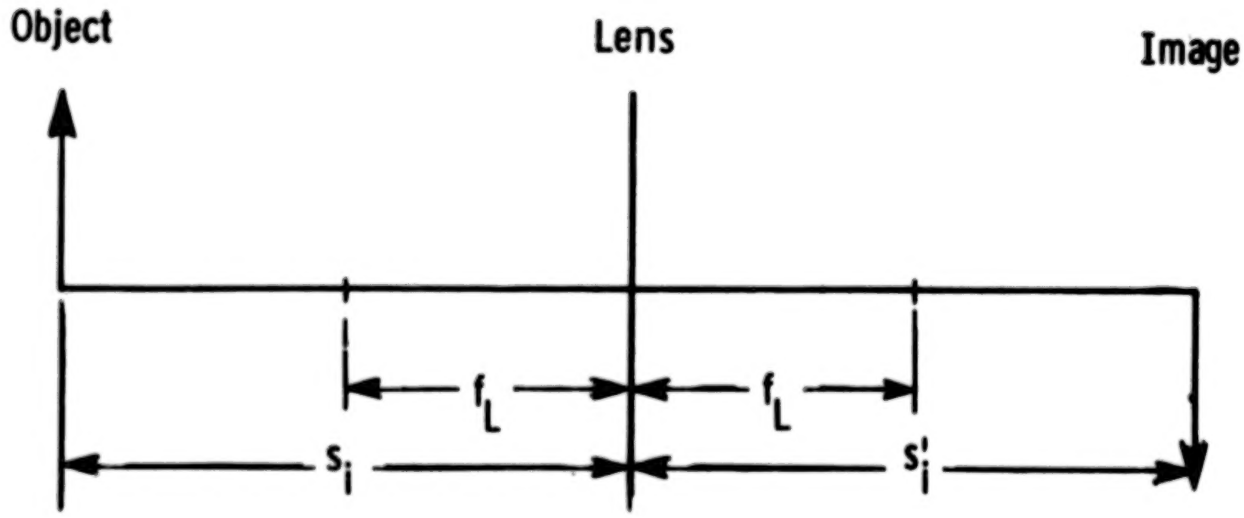

Figure 36.- Object-image conjugate relationships.

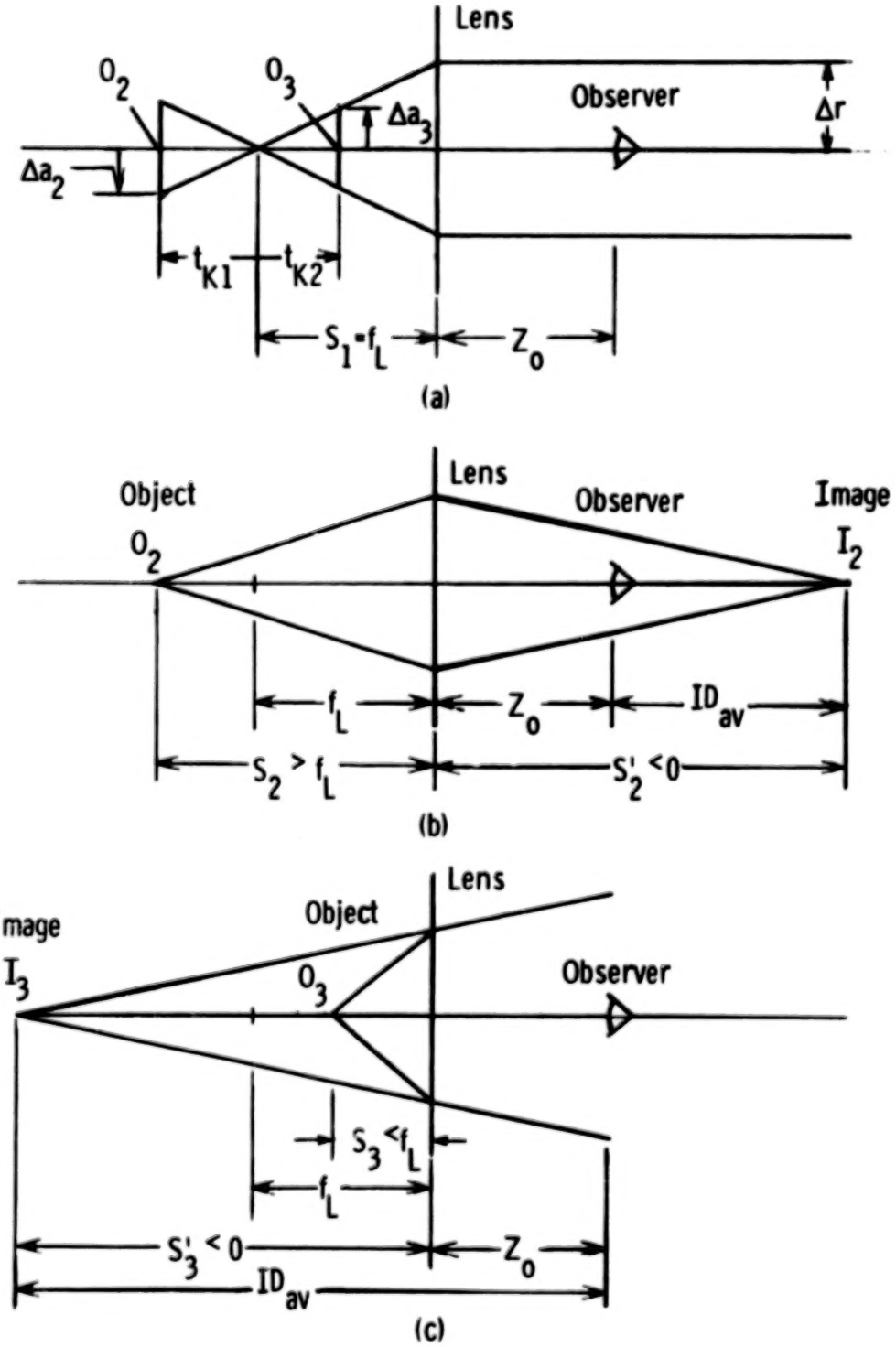

Figure 37.- Relationship between slope of aberration curve and image distance.

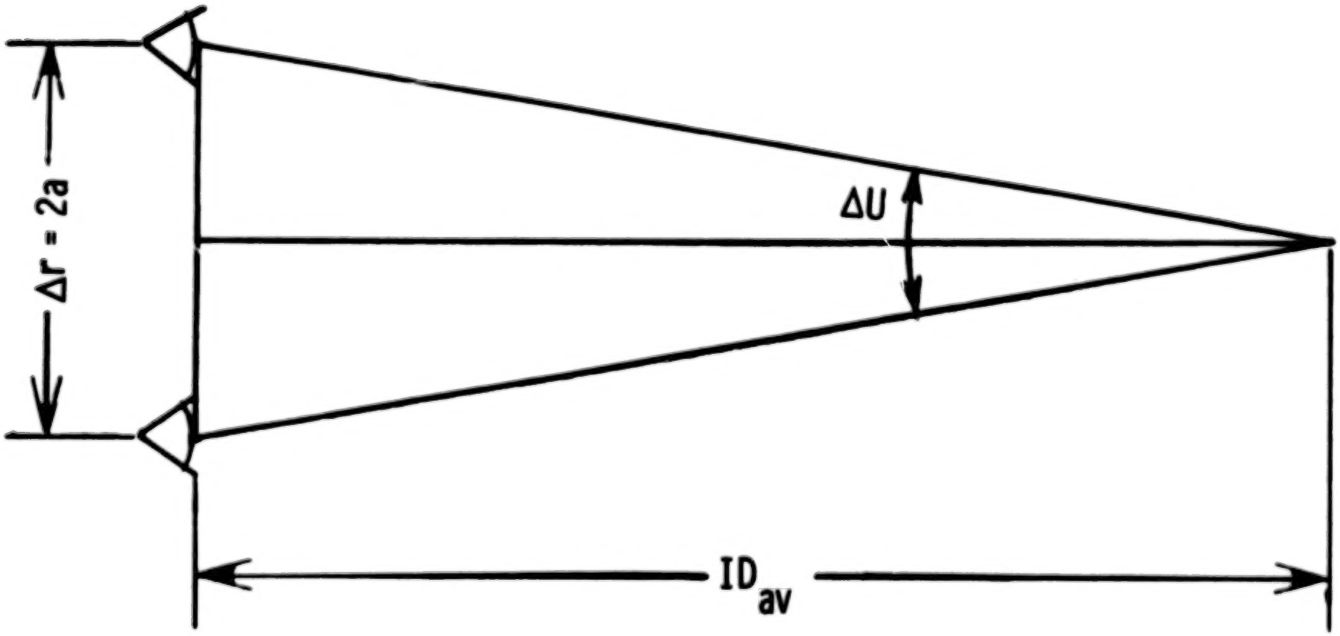

Figure 38.- Relationship between binocular disparity and image distance.

1. Report No.	2. Government Accession No.	3. Recipient's Catalog No.
NASA TP-1066		

4. Title and Subtitle	5. Report Date
ANALYSIS AND DESIGN OF A REFRACTIVE VIRTUAL IMAGE SYSTEM	November 1977
	6. Performing Organization Code

7. Author(s)	8. Performing Organization Report No.
William M. Kahlbaum, Jr.	L-11678
	10. Work Unit No. 992-16-05-03

9. Performing Organization Name and Address	11. Contract or Grant No.
NASA Langley Research Center Hampton, VA 23665	
	13. Type of Report and Period Covered Technical Paper

12. Sponsoring Agency Name and Address	14. Sponsoring Agency Code
National Aeronautics and Space Administration Washington, DC 20546	

15. Supplementary Notes

16. Abstract

This paper describes the development of analytical tools for evaluating the optical performance of a virtual image display system. Observation of a two-element (unachromatized doublet) refractive system led to the conclusion that the major source of image degradation was lateral chromatic aberration. This conclusion was verified by computer analysis of the system. The lateral chromatic aberration is given in terms of the resolution of the phosphor dots on a standard shadow mask color cathode ray tube (CRT). Single wavelength considerations include: astigmatism, apparent image distance from the observer, binocular disparities and differences of angular magnification of the images presented to each of the observer's eyes. Where practical, these results are related to the performance of the human eye. All these techniques are applied to the previously mentioned doublet and a triplet (three-element) refractive system. The triplet (a result of the design procedure described in an appendix) provides a 50-percent reduction in lateral chromatic aberration which was the design goal. Distortion was also reduced to a minimum over the field of view.

The methods used in the design of the triplet are presented along with a method of relating classical aberration curves to image distance and binocular disparity. The triplet system has been fabricated and is currently being used to provide a simulated "out the window" display for aeronautical researchers at Langley Research Center.

17. Key Words (Suggested by Author(s))	18. Distribution Statement
Visual flight simulator Lens design	Unclassified - Unlimited Subject Category 74

19. Security Classif. (of this report)	20. Security Classif. (of this page)	21. No. of Pages	22. Price*
Unclassified	Unclassified	74	$4.50

*For sale by the National Technical Information Service, Springfield, Virginia 22161

NASA-Langley, 1977